



ATLAS NOTE

ATLAS-CONF-2014-018

May 12, 2014
Minor revision: May 14, 2014



Tagging and suppression of pileup jets with the ATLAS detector

The ATLAS Collaboration

Abstract

The suppression of pileup jets has been a crucial component of many physics analyses using 2012 LHC proton-proton collisions. In ATLAS, tracking information has been used to calculate a variable called the jet-vertex-fraction, which is the fraction of the total momentum of tracks in the jet which is associated with the primary vertex. Imposing a lower limit on this variable rejects the majority of pileup jets, but leads to hard-scatter jet efficiencies that depend on the number of reconstructed primary vertices in the event (N_{Vtx}). In this note, new track-based variables to suppress pileup jets are developed in such a way that the resulting hard-scatter jet efficiency is stable as a function of N_{Vtx} . A multivariate combination of two such variables called the jet-vertex-tagger (JVT) is constructed. The modeling of JVT is tested in $Z(\rightarrow \mu\mu)+\text{jets}$ as well as in semileptonic $t\bar{t}$ events. The efficiencies of different JVT criteria are measured in data and compared to simulation. In addition, it is shown that jet-vertex association can be applied to large- R jets, providing a track-based grooming technique that is as powerful as calorimeter-based trimming but based on complementary tracking information. Finally, the performance of track-based grooming is compared with the recently proposed jet cleansing algorithm.

Revised figure 18 with respect to the version of May 12, 2014



1 Introduction

At the Large Hadron Collider (LHC) the collisions of proton (p) bunches result not only in hard-scatter (signal) pp interactions, but also in additional collisions accompanying the signal. Such additional low transverse momentum pp collisions are referred to as *pileup* interactions. We differentiate between *in-time* and *out-of-time* pileup. While in-time pileup arises from additional pp interactions in the current bunch-crossing, out-of-time pileup refers to energy deposits in the ATLAS calorimeter [1] from previous and following bunch crossings relative to the triggered event. For this note, in-time and out-of-time pileup will be referred to collectively as pileup.

The additional transverse energy flow from pileup interactions is typically subtracted on average from the signal interaction of interest. Local fluctuations in the pileup activity, however, may result in spurious pileup jets. In Ref. [2] it was shown that pileup jets can be effectively removed by a minimal jet-vertex-fraction (JVF) requirement. The JVF variable is defined as the scalar transverse momentum (p_T) sum of the tracks that are associated with the jet and originate from the hard-scatter vertex divided by the scalar p_T sum of all associated tracks:

$$\text{JVF} = \frac{\sum_k p_T^{\text{trk}_k}(\text{PV}_0)}{\sum_l p_T^{\text{trk}_l}(\text{PV}_0) + \sum_{n \geq 1} \sum_l p_T^{\text{trk}_l}(\text{PV}_n)} \quad (1)$$

Here, PV_0 is the hard-scatter vertex (see section 2.2) and PV_j , $j \geq 1$ corresponds to primary vertices due to pileup interactions in the same bunch crossing. JVF is bound between 0 and 1, but a value of -1 is assigned to jets with no associated tracks. It measures the fractional p_T from tracks associated with the hard-scatter vertex. As the denominator of JVF increases with the number of reconstructed primary vertices in the event (N_{Vtx} ¹), due to an increase in the number of pileup tracks associated with the jet, the mean JVF for signal jets is shifted to smaller values, as shown in Fig. 1(a). The explicit pileup dependence of JVF results in an N_{Vtx} dependent jet efficiency when a minimal JVF criterion is imposed to reject pileup jets. This effect is illustrated in Figure 1(b) for jets in three different p_T bins requiring $\text{JVF} > 0.5$.

In this note, new track-based variables are developed to suppress pileup jets in such a way that the resulting hard-scatter jet efficiency is stable as a function of N_{Vtx} . The note is organized as follows. In Section 2 a brief description of the ATLAS experiment is presented and the object reconstruction and event selection is discussed. Two new track-based variables are introduced in Section 3, and in Section 4 a multivariate combination of these two variables, called the *jet-vertex-tagger*, is derived and its performance is characterized. The modeling of the jet-vertex-tagger is validated with data in Section 5. In Section 6 the application of the jet-vertex-tagger is illustrated in a study of the jet multiplicity in $Z(\rightarrow \mu\mu)$ +jets events as well as for a jet-veto efficiency study in simulated $H \rightarrow ZZ$ events, where the Higgs boson H is produced via vector-boson fusion ($qq' \rightarrow qq'H$). Section 7 contains a discussion of a novel track-based grooming technique for large- R jets, where jet-vertex association is used to mitigate pileup effects. Finally, Section 8 contains the conclusions.

2 Object definition and event selection

2.1 The ATLAS detector

The results presented in this paper are based on an integrated luminosity of 20.3 fb^{-1} of pp collisions recorded with the ATLAS detector at a center-of-mass energy of 8 TeV during the 2012 data taking.

¹The vertex reconstruction efficiency depends on the average number of interactions per bunch crossing μ and ranges between 80% and 50% for $\mu = 0$ to $\mu = 40$ [3].

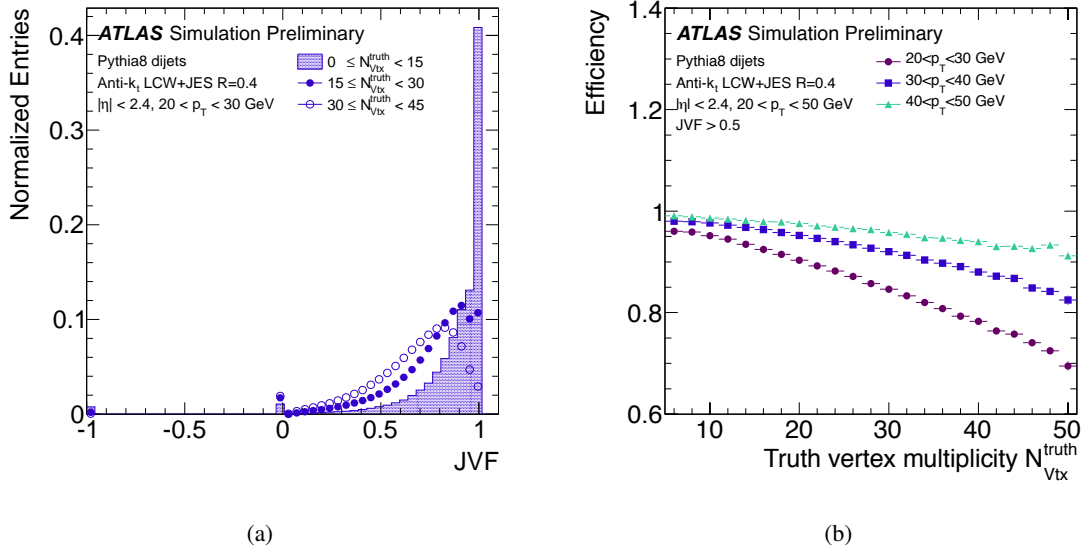


Figure 1: (a) The JVF distribution for hard-scatter jets (see Section 2.2) in simulated dijet events for different bins in truth vertex multiplicity N_{Vtx}^{truth} . (b) The efficiency of a JVF > 0.5 requirement for hard-scatter jets as a function of N_{Vtx}^{truth} , for three different jet p_T bins.

ATLAS is a cylindrical multi-purpose particle detector hermetic in azimuth for a pseudorapidity² range of $|\eta| < 4.9$. It comprises an inner tracking detector, electromagnetic and hadronic sampling calorimeters, and an air-toroid muon system. The inner detector, which includes the silicon pixel detector, a silicon microstrip detector and a transition radiation tracker, covers a pseudorapidity range $|\eta| < 2.5$ and is immersed in a 2 T axial magnetic field produced by a superconducting solenoid. Surrounding the solenoid there are finely-segmented liquid argon and iron-scintillator calorimeters providing precise energy measurements. Outside the calorimetry there is a muon spectrometer immersed in a magnetic field provided by three large toroid magnets. A multi-level trigger system of dedicated hardware and software filters is used to select pp collisions. A detailed description of the ATLAS detector can be found elsewhere [1].

2.2 Object reconstruction

The reconstruction and definition of physics objects used in this analysis is based on Ref. [2], where more details can be found.

Vertices and tracks

The event hard-scatter primary vertex is defined as the one reconstructed vertex with the largest $\sum p_T^2$ of constituent tracks. Tracks are selected with $p_T > 0.5$ GeV and are further required to pass quality criteria designed to reject poorly measured and fake tracks. A careful association of tracks to vertices is crucial to optimize the separation between pileup and hard-scatter jets. We use the following two-step procedure. First, tracks are assigned to vertices based on the track-to-vertex association resulting from the vertex reconstruction [3]. Secondly, tracks that have a $|z_0| < 3$ mm with respect to the hard-scatter primary

² ATLAS uses a right-handed coordinate system with its origin at the nominal interaction point (IP) in the centre of the detector and the z -axis along the beam pipe. The x -axis points from the IP to the centre of the LHC ring, and the y -axis points upward. Cylindrical coordinates (r, ϕ) are used in the transverse plane, ϕ being the azimuthal angle around the beam pipe. The pseudorapidity is defined in terms of the polar angle θ as $\eta = -\ln \tan(\theta/2)$.

vertex and are not associated with any vertex after the first step are then assigned to the hard-scatter primary vertex. This additional step is important for jets that are initiated by heavy flavor quarks, where tracks may arise from hadron decays in flight. The details of this two-step track-to-vertex association are discussed in Appendix A. Tracks originating from the hard-scatter primary vertex and from pileup vertices are then assigned to jets using a technique known as ghost association [4] which is described in Ref. [2].

Jets

Calorimeter jets are reconstructed from topological clusters [5] using the local cluster weighting (LCW) algorithm [6]. FASTJET 2.4.3 is used to reconstruct anti- k_t [7] jets with a distance parameter $R = 0.4$. Similarly, truth jets are reconstructed as anti- k_t $R = 0.4$ jets from stable truth particles in the final state of the simulated hard-scatter interaction. Calorimeter jets are calibrated using pileup subtraction followed by a jet-energy-scale (JES) response correction, as described in detail in Refs. [2, 8]. Unless noted otherwise, jets are required to have $20 < p_T < 50$ GeV and to be within $|\eta| < 2.4$ so that their charged particles are within the coverage of the inner tracking detector. Large- R jets are reconstructed from LCW topological clusters using the anti- k_t algorithm with $R = 1.0$. The jet mass is defined as the mass deduced from the four-momentum sum of all jet constituents.

Similarly to Ref. [2], pileup and hard-scatter jets are defined for simulated events by a matching criterion to truth jets reconstructed from stable, interacting³ particles in the final state of the hard-scatter interaction. Signal jets are matched within $\Delta R = \sqrt{(\Delta\eta)^2 + (\Delta\phi)^2} < 0.3$ to a truth jet with $p_T > 10$ GeV⁴. Unless noted otherwise, pileup jets are required to have a minimal $\Delta R > 0.6$ from any truth jet with $p_T > 4$ GeV. The pileup jet rates as a function of jet p_T and η are shown in Appendix B.

2.3 Samples and event selection

For this study, single muon triggers with a p_T threshold of 24 and 36 GeV (isolation criteria are applied at the lower threshold) were used in data and simulation to obtain an event selection dominated by either $Z(\rightarrow \mu\mu)$ +jets or $t\bar{t}$ events.

Reconstructed events containing an opposite-sign di-muon pair consistent with the Z -boson mass constraint are selected for the sample of $Z(\rightarrow \mu\mu)$ +jets events. A sample of $t\bar{t} \rightarrow (W \rightarrow \mu\nu)(W \rightarrow qq')b\bar{b}$ events is obtained with a purity of at least 90% by adopting the event selection from Ref. [9]. Most importantly, events are required to contain exactly one isolated $p_T > 25$ GeV muon with $|\eta| < 2.4$, have missing transverse energy $E_T^{\text{miss}} > 20$ GeV and two $p_T > 25$ GeV b -tagged jets identified using the 70% working point of the “MV1” b -tagging discriminant [10]. Furthermore, there must be at least two additional jets with $p_T > 25$ GeV that have a dijet invariant mass consistent with the W -boson mass.

For the performance studies based on simulated QCD dijet events in Sections 3 and 4, the reconstructed hard-scatter primary vertex is required to lie within $|\Delta z| < 0.1$ mm of the generated hard-scatter vertex.

Simulated $t\bar{t}$ events were generated with PowHEG V1.0 [11, 12, 13] using the PDF set CT10 [14]. PYTHIA 6.4 [15] was used for fragmentation and hadronization with the Perugia2011C [16] tune that employs the LO CTEQ6L1 PDF set [17]. The single top s - and Wt -channel production is modelled in the same way, while for the t -channel production AcerMC [18] and the CTEQ6L1 PDF set are used, interfaced with PYTHIA using the Perugia2011C tune. SHERPA 1.4.1 [19] is used for the matrix-element

³ Truth particles are considered stable if their decay length $c\tau$ is greater than 1 cm. A truth particle is considered to be interacting if it is expected to deposit most of its energy in the ATLAS calorimeters; muons and neutrinos are considered to be non-interacting.

⁴The $p_T > 10$ GeV threshold is used to avoid accidental matches of reconstructed jets with soft activity from the truth hard-scatter.

generation as well as for the modeling of the parton shower and hadronization of $Z(\rightarrow \mu\mu)$ +jets events. Additionally, an alternative sample of $Z(\rightarrow \mu\mu)$ +jets events is generated with PowHEG V1.0 and showered with PYTHIA8 [20]. W +jets production is based on ALPGEN V2.14 [21], with the parton shower modelled with PYTHIA 6.4 and the Perugia2011C tune. QCD dijet events are produced with the PYTHIA8 generator (version 8.160) using the CT10 PDF set and the AU2 CT10 underlying-event tune [22]. The effect of pileup jet suppression is studied in an example physics case using a sample of $qq' \rightarrow Hqq'$, $H \rightarrow ZZ$. These events are produced using PowHEG interfaced with PYTHIA8, using the CT10 PDF set and the AU2 CT10 underlying-event tune. The use of tracking information to suppress pileup jets in large- R jets is studied using a simulated sample of $W' \rightarrow WZ \rightarrow qqqq$ events with a W' mass of 1 TeV, generated with PYTHIA8 and the MSTW 2008 PDF set [23].

For all samples of simulated events, the effect of in-time as well as out-of-time pileup is simulated using minimum-bias events generated with PYTHIA8 to reflect the pileup conditions during the 2012 data-taking period. All generated events were processed with a detailed simulation of the ATLAS detector response [24] based on GEANT4 [25] and subsequently reconstructed and analyzed in the same way as the data.

3 New variables

Two new variables to separate hard-scatter (HS) from pileup (PU) jets are introduced: corrJVF, which is a pileup-corrected JVF variable, and R_{pT} , which combines both calorimeter and tracking information.

3.1 corrJVF

The quantity corrJVF is a variable similar to JVF, but corrected for the N_{Vtx} dependent average scalar sum p_T from pileup tracks associated with a jet ($\langle p_T^{PU} \rangle$). It is defined as

$$\text{corrJVF} = \frac{\sum_k p_T^{\text{trk}_k}(\text{PV}_0)}{\sum_l p_T^{\text{trk}_l}(\text{PV}_0) + \frac{\sum_{n \geq 1} \sum_l p_T^{\text{trk}_l}(\text{PV}_n)}{(k \cdot n_{\text{trk}}^{\text{PU}})}}. \quad (2)$$

where $\sum_k p_T^{\text{trk}_k}(\text{PV}_0)$ is the scalar p_T sum of the tracks that are associated with the jet and originate from the hard-scatter vertex. The term $p_T^{\text{PU}} = \sum_{n \geq 1} \sum_l p_T^{\text{trk}_l}(\text{PV}_n)$ denotes the scalar p_T sum of the associated tracks that originate from any of the pileup interactions. To correct for the linear increase of $\langle p_T^{PU} \rangle$ with the total number of pileup tracks per event ($n_{\text{trk}}^{\text{PU}}$), we divide p_T^{PU} in the corrJVF definition by $(k \cdot n_{\text{trk}}^{\text{PU}})$ with $k = 0.01$. The total number of pileup tracks per event is computed from all tracks associated with vertices other than the hard-scatter vertex. The scaling factor k is roughly taken as the slope of $\langle p_T^{PU} \rangle$ with $n_{\text{trk}}^{\text{PU}}$, but the resulting discrimination between hard-scatter and pileup jets is insensitive to the choice of k ⁵.

Figure 2(a) shows the corrJVF distribution for pileup and hard-scatter jets in simulated dijet events. A value corrJVF = -1 is assigned to jets with no associated tracks. About 1% of hard-scatter jets with $20 < p_T < 30$ GeV have no associated hard-scatter tracks and thus corrJVF = 0.

Figure 2(b) shows the hard-scatter jet efficiency as a function of the number of reconstructed primary vertices in the event when imposing a minimal corrJVF or JVF requirement such that the N_{Vtx} inclusive efficiency is 90%. For the full range of N_{Vtx} considered, the hard-scatter jet efficiency after a selection based on corrJVF is stable at $90\% \pm 1\%$, whereas for JVF the efficiency degrades by about 20%, from 97% to 75%. The choice of the scaling factor k in the corrJVF distribution does not affect the stability of the hard-scatter jet efficiency with N_{Vtx} .

⁵With this particular choice of k , the resulting corrJVF shapes for hard-scatter and pileup jets are similar to the corresponding ones of JVF.

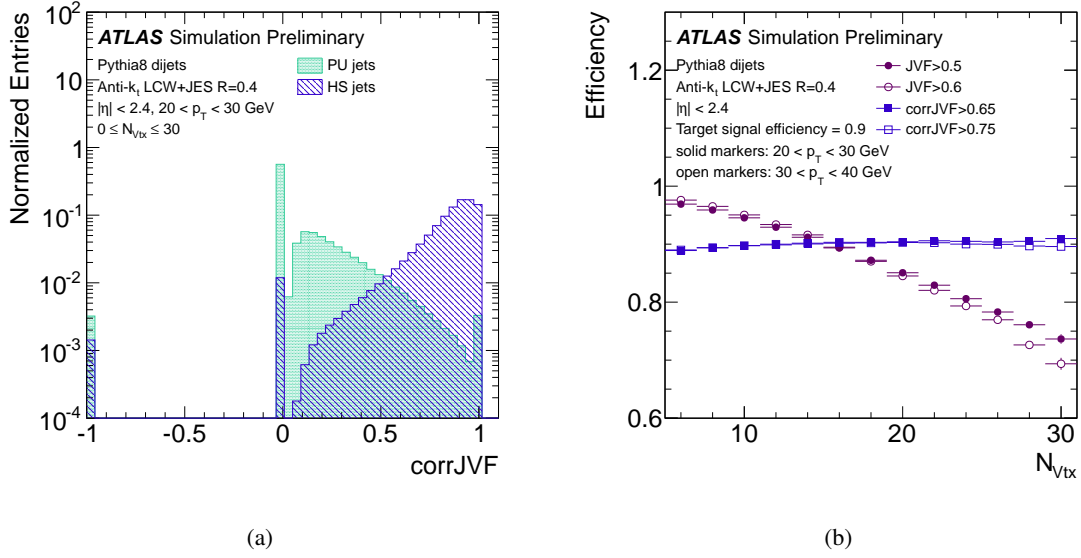


Figure 2: (a) Distribution of corrJVF for pileup and hard-scatter jets with $20 < p_T < 30$ GeV. (b) Primary-vertex dependence of the hard-scatter jet efficiency for $20 < p_T < 30$ GeV (solid markers) and $30 < p_T < 40$ GeV (open markers) jets for fixed cuts of corrJVF (blue) and JVF (violet) such that the inclusive efficiency is 90%. The cut values imposed on corrJVF and JVF, which depend on the p_T bin, are specified in the legend.

3.2 R_{pT}

The variable R_{pT} is defined as the scalar p_T sum of the tracks that are associated with the jet and originate from the hard-scatter vertex divided by the fully calibrated jet p_T , which includes pileup subtraction:

$$R_{pT} = \frac{\sum_k p_T^{\text{trk}_k}(\text{PV}_0)}{p_T^{\text{jet}}}. \quad (3)$$

R_{pT} is peaked at 0 and steeply falling for pileup jets, where no or only little p_T from tracks from the hard-scatter vertex is expected. For hard-scatter jets, however, R_{pT} has the meaning of a charged p_T fraction and its mean value and spread is larger than for pileup jets. Since R_{pT} involves only tracks that are associated with the hard-scatter vertex, its definition is at first order independent of N_{Vtx} . The R_{pT} distributions for pileup and hard-scatter jets are shown in Figure 3(a). Figure 3(b) shows the hard-scatter jet efficiency as a function of N_{Vtx} when imposing a minimal R_{pT} and JVF requirement such that the N_{Vtx} inclusive efficiency is 90%. For the full range of N_{Vtx} considered, the hard-scatter jet efficiency after a selection based on R_{pT} is stable at $90\% \pm 1\%$.

Figures 4(a) and 4(b) show the 2-dimensional correlation of R_{pT} and corrJVF for hard-scatter and pileup jets, respectively. Hard-scatter jets are characterized by large corrJVF and large R_{pT} , whereas pileup jets are concentrated at low R_{pT} and low corrJVF values. Jets with $\text{corrJVF} = -1$ (i.e. no associated tracks) or $R_{pT} > 1.5$ are omitted in these plots. Most pileup jets (and about 1% of hard-scatter jets) have no tracks that originate from the hard-scatter vertex and thus $\text{corrJVF} = R_{pT} = 0$.

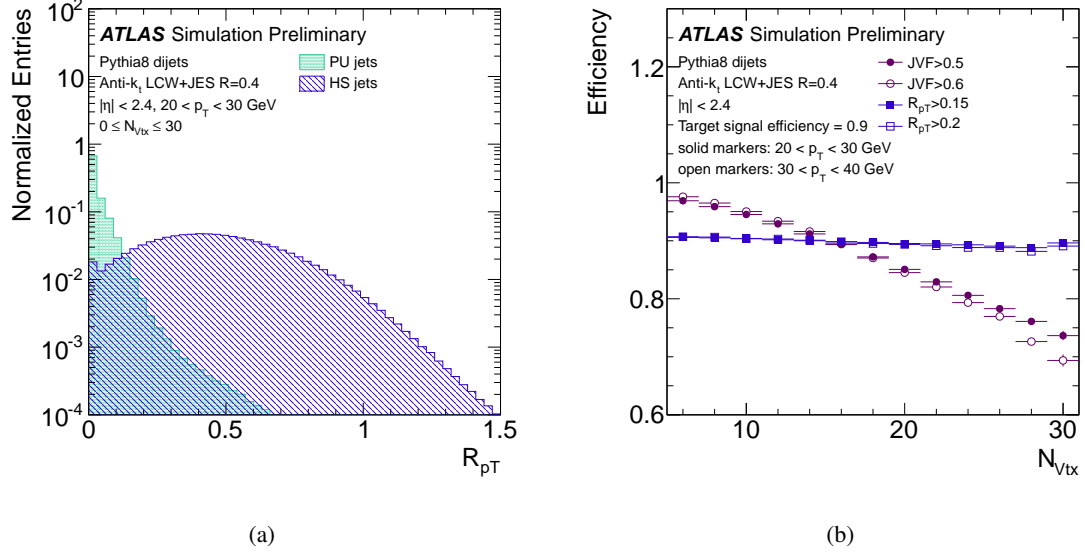


Figure 3: (a) Distribution of R_{pT} for pileup and hard-scatter jets with $20 < p_T < 30$ GeV. (b) Primary-vertex dependence of the hard-scatter jet efficiency for $20 < p_T < 30$ GeV (solid markers) and $30 < p_T < 40$ GeV (open markers) jets for fixed cuts of R_{pT} (blue) and JVF (violet) such that the inclusive efficiency is 90%. The cut values imposed on R_{pT} and JVF, which depend on the p_T bin, are specified in the legend.

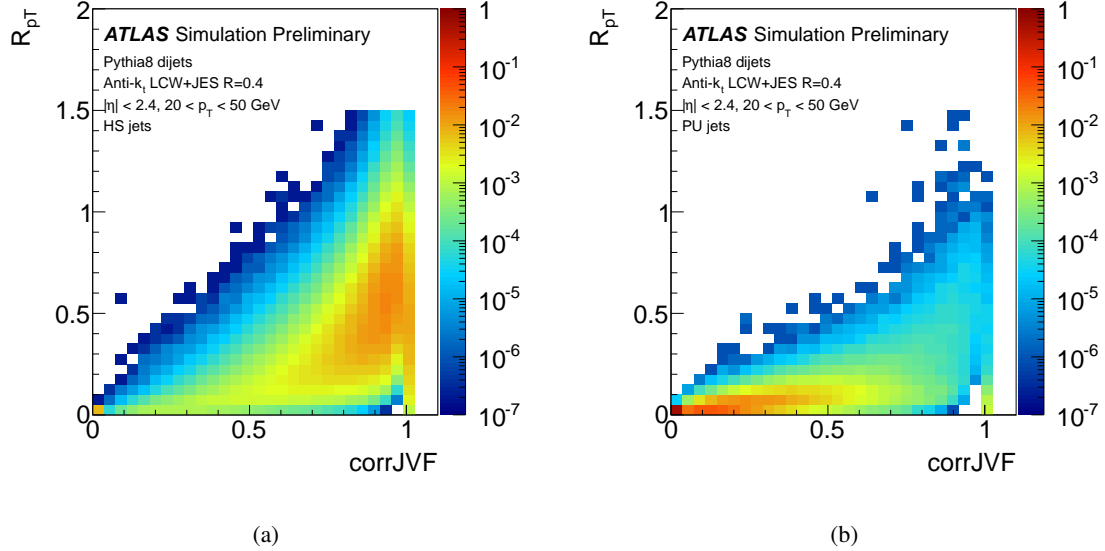


Figure 4: 2-dimensional correlation of $corrJVF$ and R_{pT} for hard-scatter (a) and pileup (b) jets.

4 The jet-vertex-tagger

4.1 Derivation of the discriminant

A new discriminant called the jet-vertex-tagger (JVT) is constructed using R_{pT} and corrJVF as a 2-dimensional likelihood, based on a k-nearest neighbor (kNN) algorithm [26]. For each point in the two-dimensional corrJVF – R_{pT} plane, the relative probability for a jet at that point to be of signal type is computed as the ratio of the number of hard-scatter jets divided by the number of hard-scatter plus pileup jets found in a local neighborhood around the point using a training sample of signal and pileup jets with $20 < p_T < 50$ GeV and $|\eta| < 2.4$. The local neighborhood is defined dynamically as the 100 nearest neighbors around the test point using a Euclidean metric in the R_{pT} – corrJVF space, where corrJVF and R_{pT} are rescaled so that the variables have the same width. Since only based on two variables, the kNN algorithm allows for a local and straightforward calculation of the relative signal probability, while largely avoiding statistical fluctuations in sparsely populated regions. The resulting 2-dimensional JVT likelihood is shown in Figure 5(a). In the following, the JVT value of a jet is calculated, based on its corrJVF and R_{pT} values, using the finely binned histogram in Figure 5(a) as a lookup table. The JVT distribution for hard-scatter and pileup jets with $20 < p_T < 30$ GeV is shown in Figure 5(b). A value of $JVT = -0.1$ is assigned to jets with no associated tracks.

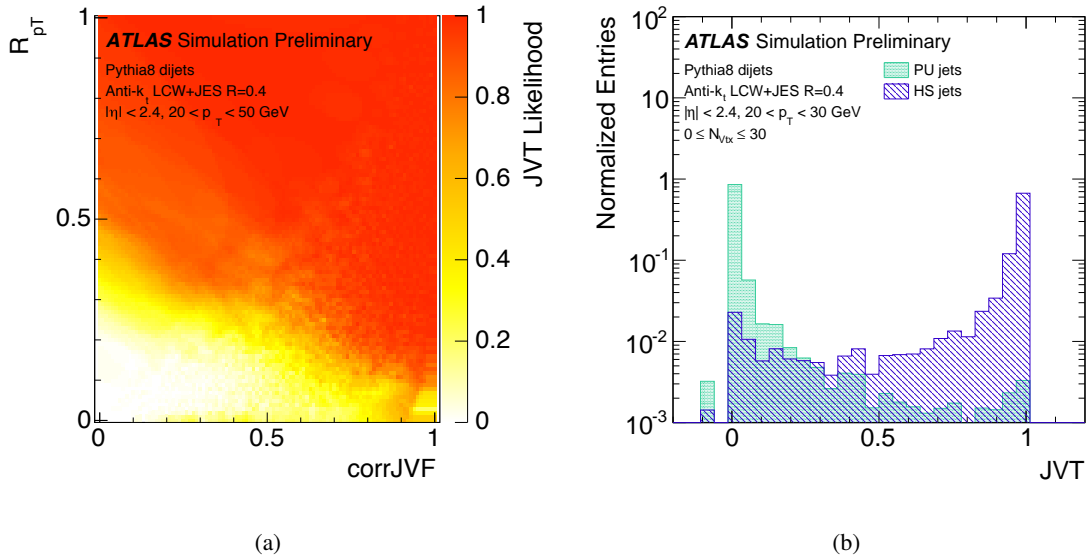


Figure 5: (a) The 2-dimensional JVT likelihood as a function of corrJVF and R_{pT} . Jets with corrJVF = -1 (i.e. no associated tracks) are omitted in this figure. Jets with $R_{pT} > 1$ have JVT from 0.98 to 1 and are not included in the figure. (b) Distribution of JVT for pileup and hard-scatter jets with $20 < p_T < 30$ GeV.

To test the sample dependence of JVT, the likelihood is also derived using a sample of $20 < p_T < 50$ GeV jets in simulated $Z(\rightarrow \mu\mu)$ +jets events. The performance of the JVT-based pileup jet suppression (evaluated in terms of fake rate vs. efficiency curves) is found not to significantly depend on the sample from which the likelihood is derived. These studies are reported in Appendix C.

4.2 Performance of the JVT-based pileup jet rejection

Figure 6(a) shows the fake rate versus efficiency curves comparing the performance of the four variables JVF⁶, corrJVF, R_{pT} , and JVT when selecting a sample of jets with $20 < p_T < 50$ GeV, $|\eta| < 2.4$ in simulated dijet events. The figure shows the fraction of pileup jets passing a minimal JVF, corrJVF,

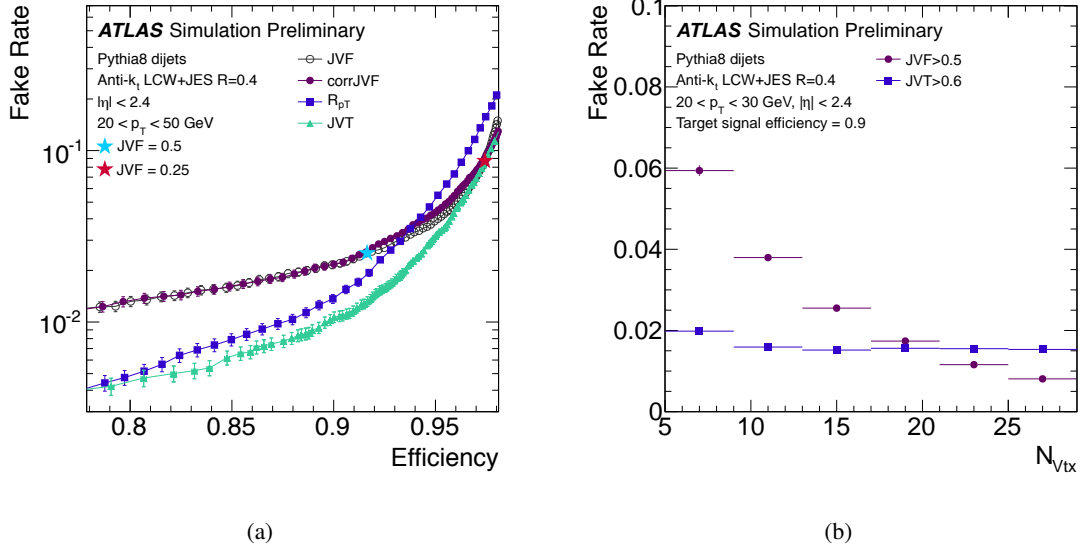


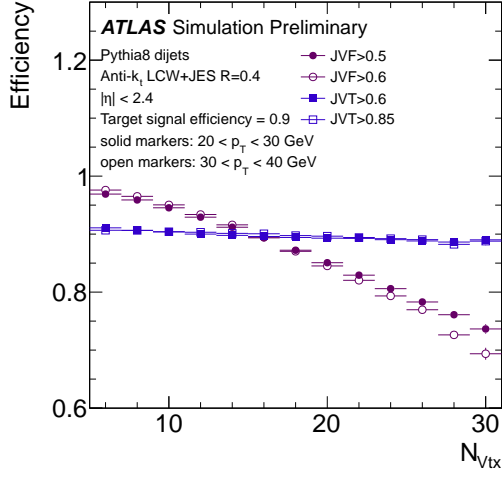
Figure 6: (a) Fake rate from pileup jets versus hard-scatter jet efficiency curves for JVF, corrJVF, R_{pT} , and JVT. The widely used JVF working points with cut values 0.25 and 0.5 are indicated with red and blue stars. (b) N_{Vtx} dependence of the pileup jet fake rate when imposing cuts on JVT (blue) and JVF (violet) such that the inclusive hard-scatter jet efficiency is 90%.

R_{pT} or JVT requirement as a function of the signal jet efficiency resulting from the same requirement. The JVT performance is driven by corrJVF (R_{pT}) in the region of high signal jet efficiency (high pileup rejection). Using JVT, signal jet efficiencies of 80%, 90% and 95% are achieved for pileup fake rates of respectively 0.4%, 1.0% and 3%. When imposing cuts on JVF that result in the same jet efficiencies, the pileup fake rates are 1.3%, 2.2% and 4%.

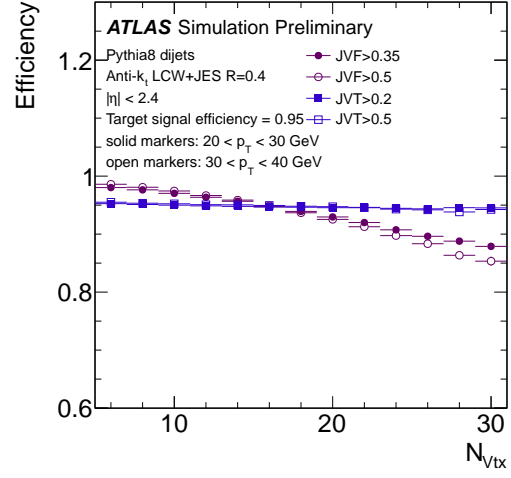
Figure 6(b) shows the pileup jet fake rate as a function of the number of reconstructed primary vertices in the event when imposing a minimal JVT and JVF requirement such that the N_{Vtx} inclusive efficiency is 90%. While for JVT the fake rate is stable, a decreasing trend with N_{Vtx} is observed for JVF, due to the pileup dependent denominator in the JVF definition (see Eqn. (1)).

The dependence of the hard-scatter jet efficiencies on N_{Vtx} is shown in Figure 7(a), when imposing the same JVF and JVT cuts as in Figure 6(b). In Figure 7(b) looser cut values are used, resulting in N_{Vtx} inclusive hard-scatter jet efficiencies of 95%. For the full range of N_{Vtx} considered, the hard-scatter jet efficiencies after a selection based on JVT are stable within 1%. Figure 8 is similar to Figure 7 but instead shows the hard-scatter jet efficiencies as a function of the average number of interactions per bunch crossing μ .

⁶The JVF definition used here is the one of Ref. [2] (i.e. based on a different track-to-vertex association), to allow for a direct comparison of the performance of the pileup jet suppression between this note and Ref. [2].

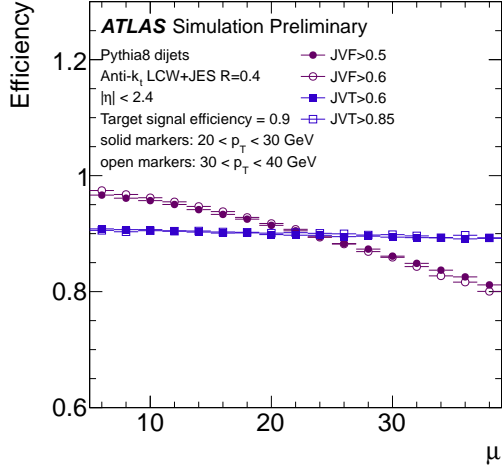


(a)

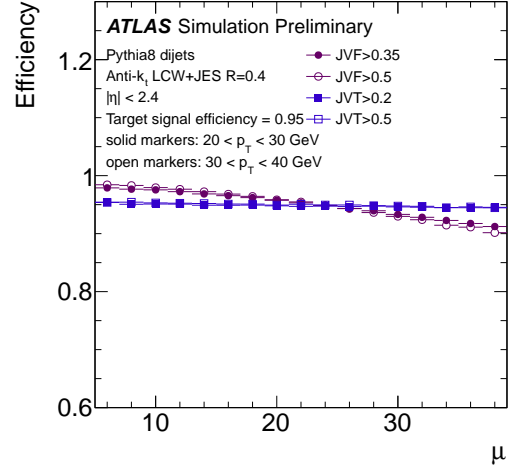


(b)

Figure 7: Primary-vertex dependence of the hard-scatter jet efficiency for $20 < p_T < 30$ GeV (solid markers) and $30 < p_T < 40$ GeV (open markers) jets for fixed cuts of JVT (blue) and JVF (violet) such that the inclusive efficiency is 90% (a) and 95% (b). The cut values imposed on JVT and JVF, which depend on the p_T bin, are specified in the legend.



(a)



(b)

Figure 8: Dependence of the hard-scatter jet efficiency for $20 < p_T < 30$ GeV (solid markers) and $30 < p_T < 40$ GeV (open markers) jets as a function of the average number of interactions per bunch crossing μ . Fixed cuts of JVT (blue) and JVF (violet) are imposed such that the inclusive efficiency is 90% (a) and 95% (b). The cut values imposed on JVT and JVF, which depend on the p_T bin, are specified in the legend.

4.3 Flavor dependence

The difference in fragmentation and showering between light-quark and gluon initiated jets is expected to affect the shapes of corrJVF and R_{pT} and thus the performance of the JVT based pileup jet suppression. The corrJVF- and R_{pT} -based discrimination between pileup and hard-scatter jets relies on the successful reconstruction and association of the hard-scatter tracks. Light (uds)-quark initiated jets have on average a lower number of associated hard-scatter tracks but a slightly higher response [27] and both effects lead towards an increase in the number of jets with no associated tracks from the hard-scatter primary vertex with respect to gluon initiated jets.

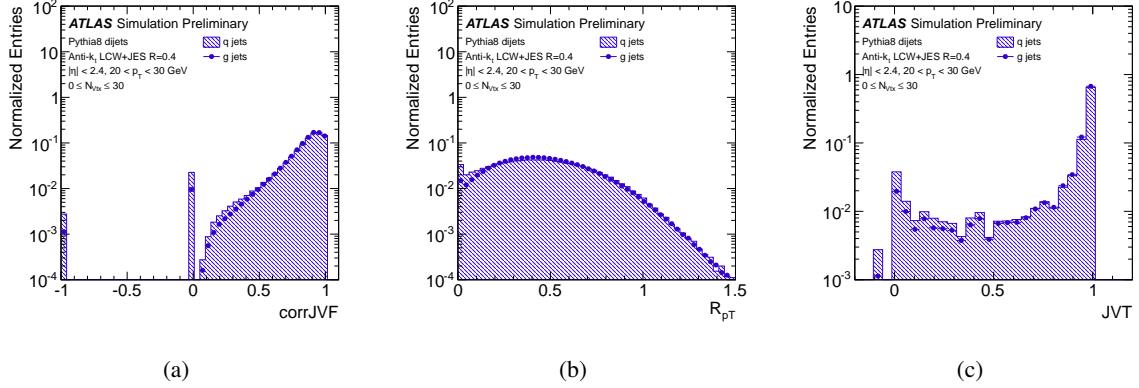


Figure 9: The distributions of corrJVF (a), R_{pT} (b) and JVT (c) for light-quark and gluon initiated hard-scatter jets.

In Fig. 9 we show the corrJVF, R_{pT} and JVT distributions for light-quark and gluon initiated hard-scatter jets with $20 < p_T < 30$ GeV. Using a leading order notion of jet flavor, the partonic flavor labeling refers to the highest energy parton within a narrow cone of $\Delta R < 0.3$ around the jet axis. The distributions for light-quark initiated jets have more entries at low corrJVF, R_{pT} and JVT values and consequently a worse separation from pileup jets. Most notably, about twice as many light-quark jets have no associated tracks from the hard-scatter primary vertex, thus $\text{corrJVF} = \text{JVT} = 0$.

Figure 10 shows the efficiency vs. fake-rate curve for JVT for light-quark, gluon and b-quark initiated jets. As expected from Figure 9, the performance is worse for light-quark initiated jets. The pileup vs. hard-scatter jet discrimination is best performing for b-quark initiated hard-scatter jets, profiting from the optimized track-to-vertex association as described in Section 2.2. It was found that the efficiency vs. fake-rate curve for c-quark labeled jets is marginally worse than the one of gluon jets. When imposing minimal corrJVF, R_{pT} or JVT criteria, the hard-scatter jet efficiencies are lower for light-quark initiated than for gluon initiated jets.

The stability of the hard-scatter efficiencies as a function of N_{Vtx} is found to be independent of the flavor of the jet initiating parton.

5 Validation of the modeling in data

5.1 Validation in $Z(\rightarrow \mu\mu)$ +jets events

The modeling of R_{pT} , corrJVF and JVT can be validated with data using a sample of $Z(\rightarrow \mu\mu)$ candidate events where kinematic selection criteria can be used to select either hard-scatter or pileup jets. In simulation, the non-Z-boson background to this event selection is negligible and thus ignored. A sample enriched in hard-scatter jets is obtained as follows: the leading jet with $20 < p_T < 50$ GeV and $|\eta| < 2.4$

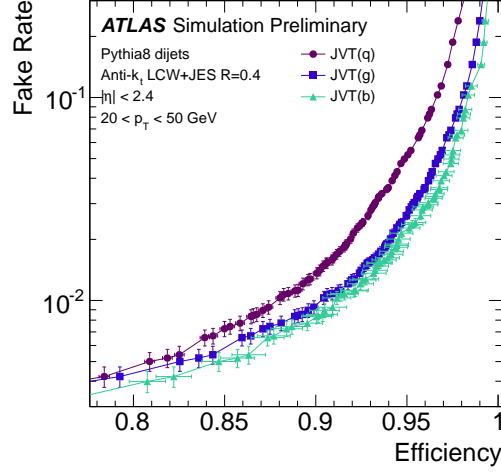


Figure 10: The fake rate from pileup jets versus hard-scatter jet efficiency curves for JVT separating light-quark, gluon and b-quark initiated jets.

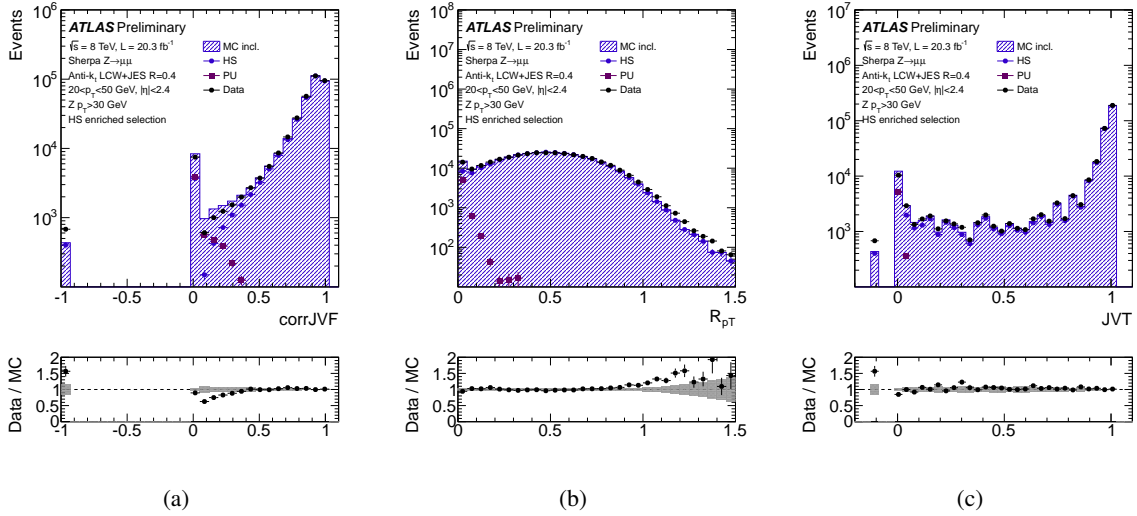


Figure 11: Comparison between data and simulation for corrJVF (a), R_{pT} (b) and JVT (c) in a hard-scatter enriched selection of jets in $Z(\rightarrow \mu\mu)+\text{jets}$ events, where a $|\Delta\phi(Z, \text{jet})| > 2.6$ requirement is imposed between the leading jet and the Z boson. The blue shaded histogram representing the inclusive simulation is subdivided in its hard-scatter jet and pileup jet contributions using blue and magenta markers respectively. The gray band in the ratio plot represents the statistical uncertainty in the simulation. The bin-by-bin variations in the JVT distribution are due to the discrete (rather than continuous) nature of the variable.

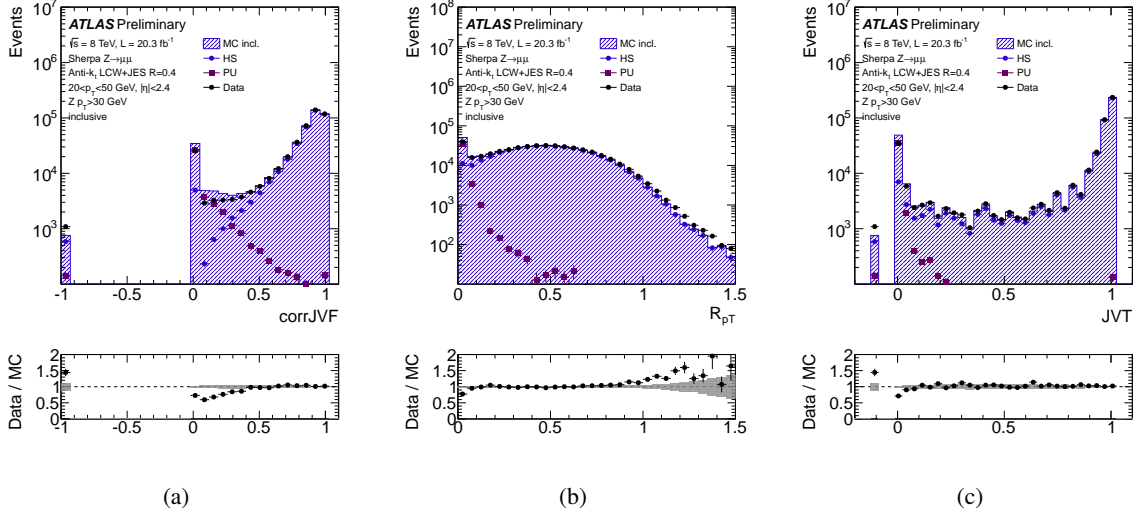


Figure 12: corrJVF (a), R_{pT} (b) and JVT (c) distributions for the leading jet with $20 < p_T < 50$ GeV and $|\eta| < 2.4$ in $Z(\rightarrow \mu\mu)+\text{jets}$ events, where the $|\Delta\phi(Z, \text{jet})|$ requirement from Figure 11 is omitted. The blue shaded histogram representing the inclusive simulation is subdivided in its hard-scatter jet and pileup jet contributions using blue and magenta markers. The gray band in the ratio plot represents the statistical uncertainty in the simulation. The bin-by-bin variations in the JVT distribution are due to the discrete (rather than continuous) nature of the variable.

is required to be azimuthally back-to-back with the reconstructed Z boson with $|\Delta\phi(Z, \text{jet})| > 2.6$. The Z-boson p_T is further required to be larger than 30 GeV. In simulation, this selection is 98% pure in hard-scatter jets. The data to simulation comparison plots for R_{pT} , corrJVF and JVT for this jet selection are shown in Figure 11. The simulation is scaled to match the data in the hard-scatter dominated region. An underestimate of the simulation in the tail of R_{pT} is observed. The minimal R_{pT} criterion used to suppress pileup jets, however, is typically around 0.2 and thus far from the mis-modelled region. Apart from an overestimate of the simulation in the pileup sensitive part of the distributions, the agreement between data and simulation is satisfactory.

Figure 12 shows the same comparison between data and simulation using a looser event selection with the $|\Delta\phi(Z, \text{jet})| > 2.6$ requirement omitted, so that the contribution from pileup jets is increased. With this selection, the pileup-jet-dominated bins are overestimated in the simulation by about 30%. The effect is most visible in the corrJVF distribution where the bins with $\text{corrJVF} \in [0, 0.3]$ have a large pileup contribution.

Next, a sample further enriched in pileup jets is obtained by imposing the same selection criteria as in Figure 11 but replacing the back-to-back requirement with the criterion $|\Delta\phi(Z, \text{jet})| < 1.2$. The data to simulation comparison for corrJVF , R_{pT} and JVT for this selection of jets is shown in Figures 13(a), 13(b) and 13(c). While the pileup dominated regions in the three distributions are overestimated in simulation, the hard-scatter dominated tails of the distributions are reasonably well reproduced.

As a cross-check, we use the simulated sample of jets passing this event selection to form a template of hard-scatter and another of pileup jets. We then perform a binned maximum likelihood fit to fit the pileup template to the data, while keeping the hard-scatter contribution at its nominal value from Figures 13(a), 13(b) and 13(c). The post-fit distributions of corrJVF , R_{pT} and JVT are shown in Figures 13(d), 13(e) and 13(f), respectively. With the rescaled pileup contribution, a good agreement between data and simulation is observed in the pileup and hard-scatter dominated regions as well as in the transition regions.

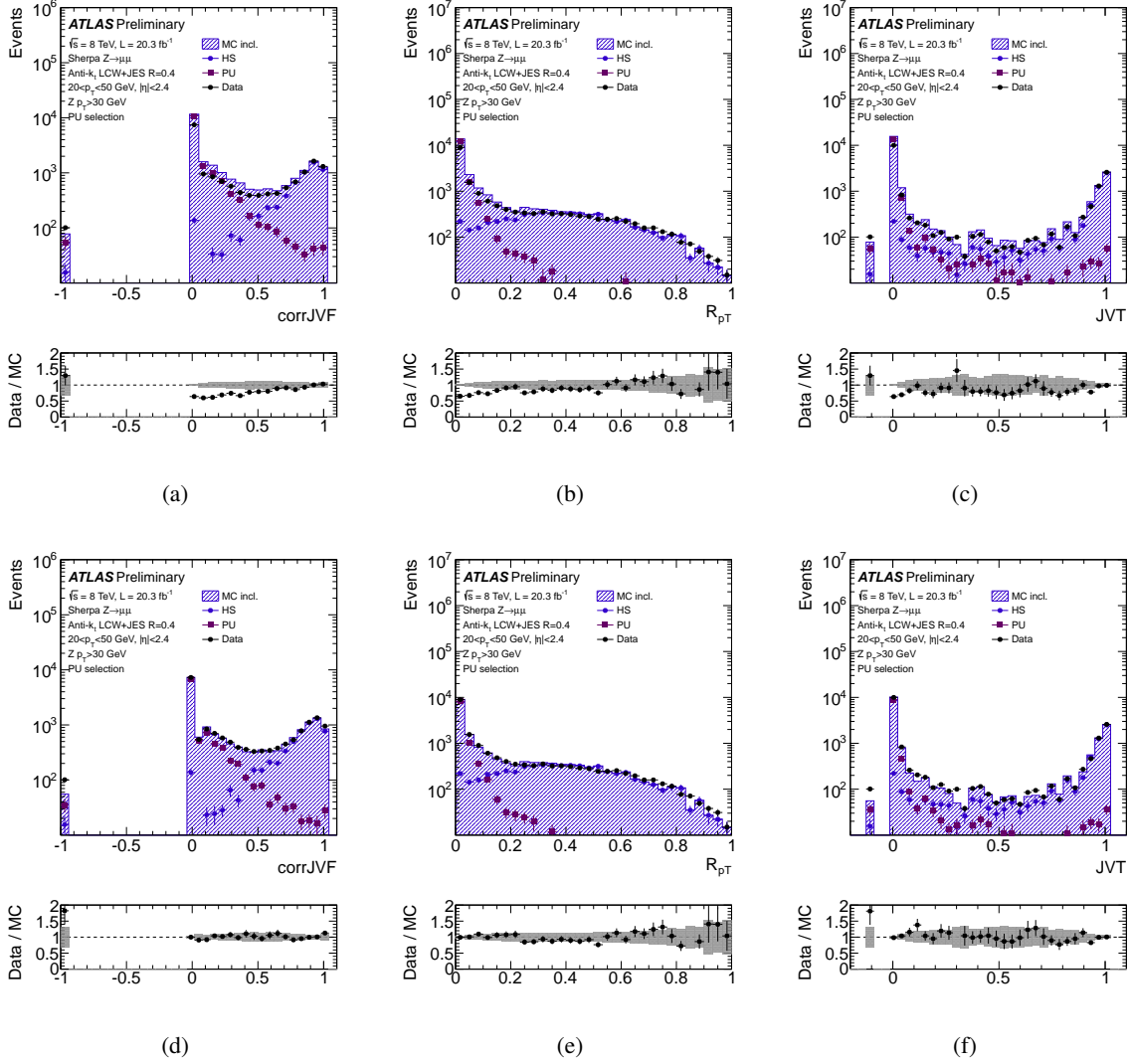


Figure 13: Distributions of corrJVF (a), R_{pT} (b) and JVT (c) using the event selection enhanced in pileup jets. In Figures (d), (e) and (f) the pileup jet contribution in the simulation it fit to the data, while keeping the hard-scatter jets at their nominal normalization.

In conclusion, the corrJVF , R_{pT} and JVT distributions of hard-scatter jets are found to be well modeled using different event selections. The pileup jet rate, however, is found to be overestimated in simulation.

5.2 Validation for b-tagged jets using $t\bar{t}$ events

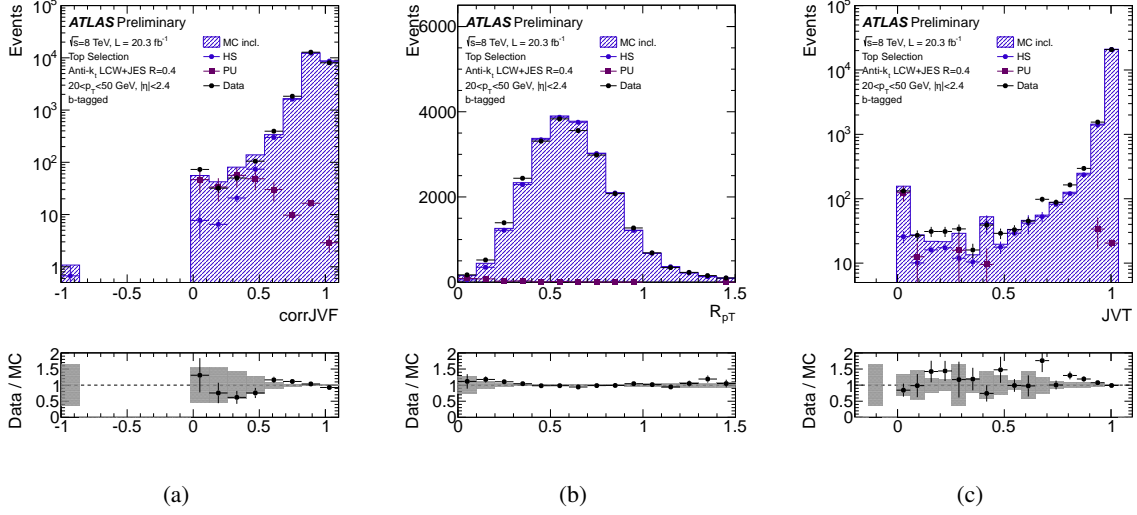


Figure 14: The distributions of corrJVF , R_{pT} and JVT for the two b-tagged jets with $20 < p_T < 50$ GeV and $|\eta| < 2.4$ in $t\bar{t}$ dominated events. The blue shaded histograms representing the inclusive simulation are subdivided in its hard-scatter jet and pileup jet contributions using blue and magenta markers respectively. The gray band in the ratio plot represents the statistical uncertainty in the simulation. The simulation is normalized to the area of the data.

Figure 14 shows a comparison of the data and the simulation for the two b-tagged jets with $20 < p_T < 50$ GeV and $|\eta| < 2.4$ in $t\bar{t}$ enriched events, using the selection described in Section 2.3. In simulation this event selection is 92% pure in $t\bar{t}$ events. A reasonable agreement is observed for the distributions of corrJVF , R_{pT} and JVT .

5.3 JVT calibration

We use jets in $Z(\rightarrow \mu\mu)$ +jets events to measure the hard-scatter jet efficiency for JVT in data, exploiting a tag-and-probe procedure similar to that described in Ref. [28]. Using the leading jet recoiling against the Z boson as a probe, a signal region of hard-scatter jets is defined as the back-to-back region specified as $|\Delta\phi(Z, \text{jet})| > 2.8$. The pileup contamination in the signal region is estimated from a pileup control region, based on the assumption that the $|\Delta\phi(Z, \text{jet})|$ distribution is flat for pileup jets. It is observed in simulation that this assumption is not well justified for the pileup jet definition given in Section 2.2. Instead, the strict requirement for pileup jets to be isolated within $\Delta R > 0.6$ from any truth jet biases the $|\Delta\phi(Z, \text{jet})|$ distribution in the back-to-back region. To avoid this problem, the isolation requirement for pileup jets is loosened to $\Delta R > 0.4$ (for which an unbiased $|\Delta\phi(Z, \text{jet})|$ distribution is found in simulation) for this efficiency measurement. The pileup control region is defined as $|\Delta\phi(Z, \text{jet})| < 1.2$ (as in Figure 13), from which the pileup contamination in the signal region $N_{\text{PU}}^{\text{signal}}$ is estimated as

$$N_{\text{PU}}^{\text{signal}}(|\Delta\phi| > 2.8) = [N_j^{\text{control}}(|\Delta\phi| < 1.2) - N_{\text{HS}}(|\Delta\phi| < 1.2)] \cdot (\pi - 2.8)/1.2, \quad (4)$$

where $N_j^{\text{control}}(|\Delta\phi| < 1.2)$ is the number of jets in the control region in the data. In simulation, the control region is about 70% pure in pileup jets, so that a remaining hard-scatter jet contamination $N_{\text{HS}}(|\Delta\phi| < 1.2)$ needs to be subtracted from the data using simulation.

The efficiency of a minimal JVT requirement is then measured in bins of $p_T^{\text{ref}} = p_T(Z)$ as

$$\varepsilon = \frac{N_j^{\text{pass}} - N_{\text{PU}}^{\text{pass}}}{N_j^{\text{signal}} - N_{\text{PU}}^{\text{signal}}} \approx \frac{N_j^{\text{pass}}}{N_j^{\text{signal}} - N_{\text{PU}}^{\text{signal}}}, \quad (5)$$

where N_j^{signal} and N_j^{pass} denote respectively the number of jets in the signal region and the number of events in the signal region passing the minimal JVT requirement. Using simulation, the contamination of pileup jets in the signal region passing the JVT cut $N_{\text{PU}}^{\text{pass}}$ is estimated to account for to less than 0.3% of N_j^{pass} for the JVT cut values considered and is thus ignored.

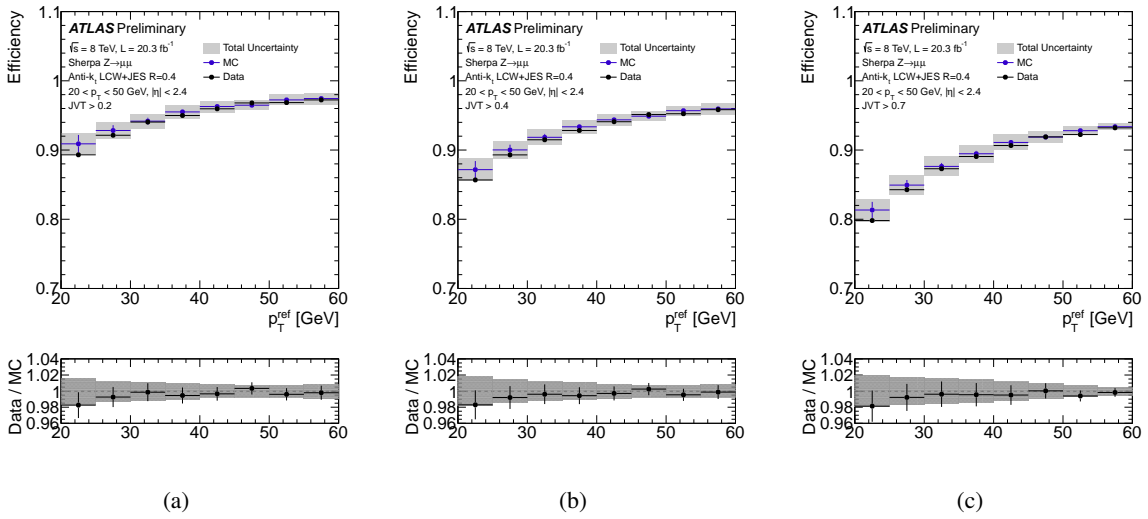


Figure 15: Efficiency of a JVT > 0.2 (a), JVT > 0.4 (b) and JVT > 0.7 (c) requirement as a function of p_T^{ref} in data and simulation.

Figures 15(a), 15(b) and 15(c) show the jet efficiencies for minimal JVT requirements of 0.2, 0.4 and 0.7 respectively. Agreement is observed between data and simulation. The simulation-to-data scale factors are consistent with unity within the uncertainties. The grey band reflects the total uncertainty on the efficiency in simulation, adding the statistical and the systematic uncertainties in quadrature. The systematic uncertainty is comprised of the following components:

- Based on a data to MC comparison of the $|\Delta\phi(Z, \text{jet})|$ distribution for jets passing a minimal JVT criterion, we assign a conservative 30% systematic uncertainty on $N_{\text{HS}}(|\Delta\phi| < 1.2)$ to account for a potential mis-modeling of the $\Delta\phi(Z, \text{jet})$ shape for hard-scatter jets.
- A non-negligible difference in hard-scatter efficiency for fixed JVT cuts is observed between the SHERPA and the POWHEG $Z(\rightarrow \mu\mu) + \text{jets}$ MC samples, attributed to the different fragmentation models used in SHERPA and PYTHIA8. This difference, which is illustrated in Figure 16, is taken as a systematic uncertainty.

The total uncertainty ranges from 2% to 1% for p_T^{ref} from 20 to 60 GeV.

Figure 17 shows the jet efficiency for minimal JVT requirements of 0.2, 0.4 and 0.7 as a function of jet η , when selecting different slices in p_T^{ref} . The total uncertainty on the measurement is slightly increased to due the slicing in one more dimension.

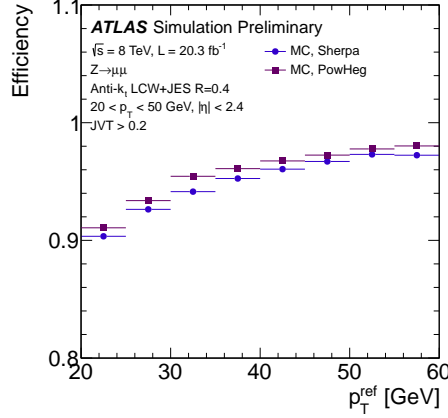


Figure 16: Comparison of the hard-scatter jet efficiency of a $JVT > 0.2$ requirement between the $Z(\rightarrow \mu\mu)$ +jets samples generated with SHERPA and POWHEG as a function of p_T^{ref} .

A $JVT > 0.4$ ($JVT > 0.7$) requirement results in efficiencies of 86% to 96% (82% to 92%) for p_T^{ref} from 20 to 60 GeV. The looser $JVT > 0.2$ requirement is about 90% efficient for $p_T = 20$ GeV jets, reaches an efficiency of at least 96% for jets with $p_T > 40$ GeV, and is thus preferable in a multi-jet environment to avoid significant efficiency losses. It should be noted that these numbers correspond to efficiencies for jets failing the pileup jet definition, which are not necessarily hard-scatter jets as defined in Section 2.2 since a few percent of jets in the signal region are classified as neither hard-scatter nor pileup jets. In simulation, the jet efficiency of a $JVT > 0.2, 0.4, 0.7$ requirements are about 1–2% higher when only using truth-matched hard-scatter jets.

6 Applications of JVT-based pileup jet suppression

6.1 Jet multiplicity in $Z(\rightarrow \mu\mu)$ +jets events

Figure 18(a) shows the average jet multiplicity $\langle N_j \rangle$ as a function of the average number of pp interactions per bunch crossing μ for $Z(\rightarrow \mu\mu)$ +jets events in data and simulation. When no selection criteria are applied to suppress pileup jets, the mean number of jets per event increases with μ at a rate that is different between data and simulation. However, the jet multiplicity is stable and independent of μ after imposing a $JVT > 0.7$ criterion. Figure 18(b) shows the change in the jet multiplicity ($\langle N_j \rangle$) with μ as a function of μ using the same selection of $Z(\rightarrow \mu\mu)$ +jets events. The slope is calculated from the difference in $\langle N_j \rangle$ between adjacent bins. When no pileup suppression criteria are applied, the graphs follow an approximately linear trend, indicating a quadratic increase in the jet multiplicity with μ . After imposing a $JVT > 0.7$ criterion, no significant change in the jet multiplicity is observed with μ for the full range of μ both for data and simulation.

6.2 Jet veto efficiency in VBF $H \rightarrow 4\ell$ events

We use a sample of simulated $qq' \rightarrow Hqq'$, $H \rightarrow ZZ \rightarrow 4\ell$, $\ell = e, \mu$, events where the Higgs boson H is produced in vector-boson fusion (VBF) to test the JVT-based pileup jet suppression for an important physics analysis that is sensitive to pileup. We adopt a similar event selection as in Ref. [29] and require the two leading jets with $p_T > 20$ GeV to be separated in η by more than 3 units. We use generator truth information to reject jets that overlap within $\Delta R < 0.4$ with the four leptonic decay products of the Higgs

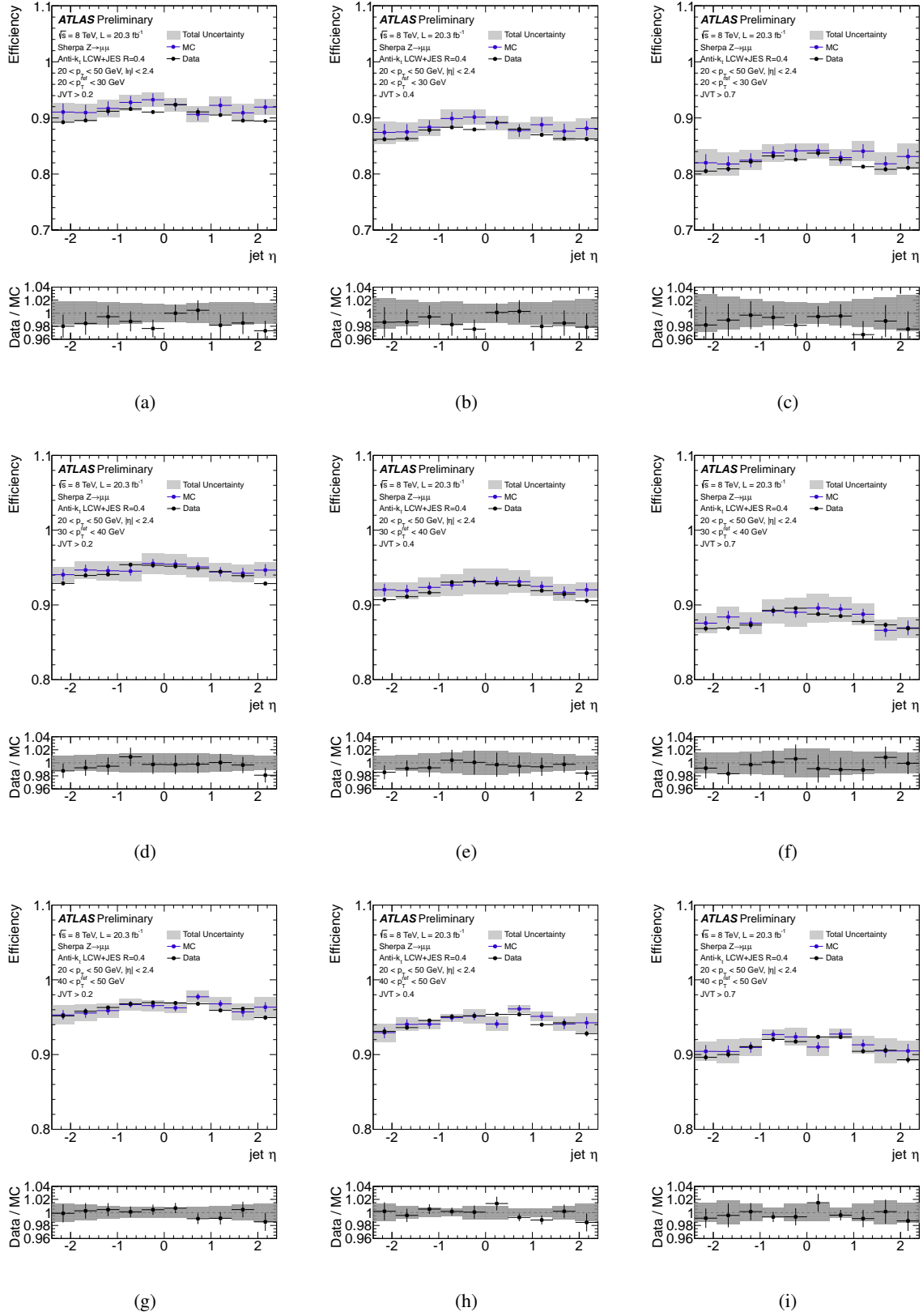


Figure 17: Efficiency of a $JVT > 0.2$ (a, d, g), $JVT > 0.4$ (b, e, h) and $JVT > 0.7$ (c, f, i) requirement as a function of jet η . The three rows represent different bins in p_T^{ref} : $20 < p_T^{\text{ref}} < 30$ GeV in (a, b, c), $30 < p_T^{\text{ref}} < 40$ GeV in (d, e, f) and $40 < p_T^{\text{ref}} < 50$ GeV in (g, h, i).

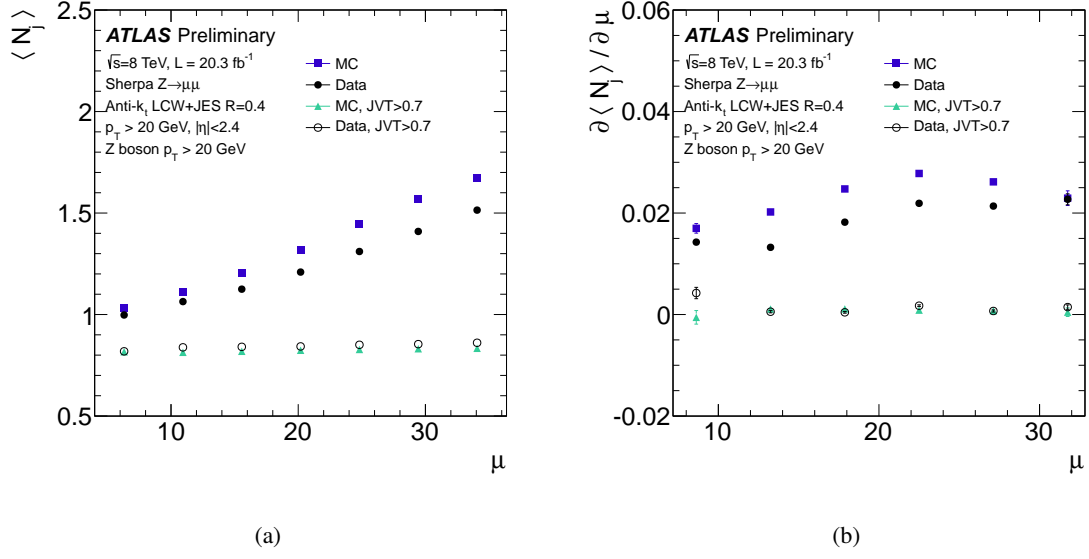


Figure 18: (a) The jet multiplicity $\langle N_j \rangle$ for jets with $p_T > 20 \text{ GeV}$ and $|\eta| < 2.4$ as a function of the average number of interactions per bunch crossing μ in $Z(\rightarrow \mu\mu)$ +jets events. (b) The change in the jet multiplicity with μ as a function of μ for the same event selection. $\langle N_j \rangle$ increases with μ at a μ dependent rate that is different for data and simulation. After imposing a $\text{JVT} > 0.7$ requirement, the number of jets is observed to be independent of μ .

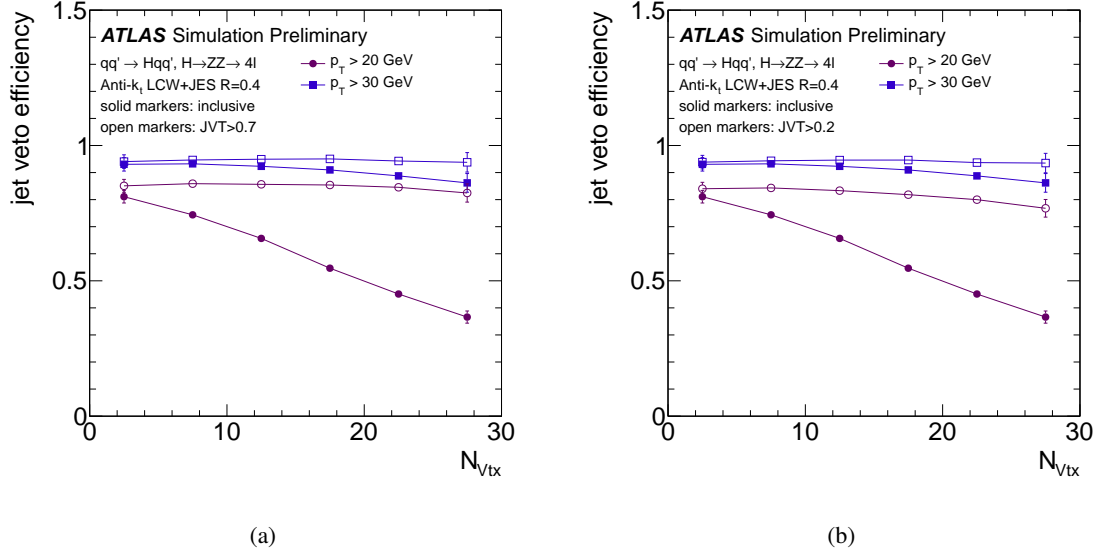


Figure 19: Event-by-event jet-veto efficiency in VBF $H \rightarrow 4\ell$ events as a function of N_{Vtx} and jet p_T threshold before and after a $\text{JVT} > 0.7$ (a) or $\text{JVT} > 0.2$ (b) criterion has been applied.

boson and require the two leading jets to originate from the selected hard-scatter vertex. The jet-veto efficiency, defined as the fraction of events in which there is no additional jet within the tracker coverage, is evaluated before and after a $JVT > 0.7$ ($JVF > 0.2$) criterion has been used to reject pileup jets. This efficiency is shown in Figure 19 as a function of jet p_T threshold and N_{Vtx} . If no pileup jet suppression is applied, the jet-veto efficiency is found to decrease from 80% to 40% and from 92% to 88% for jet veto p_T thresholds of 20 and 30 GeV, respectively, for increasing N_{Vtx} from 0 to 30. This decrease is attributed to additional jets originating from pileup interactions. When applying a $JVT > 0.7$ criterion, the jet-veto efficiency is stable at $85 \pm 2\%$ and $94 \pm 2\%$ for the same p_T thresholds. Using the looser $JVT > 0.2$ criterion, a marginal N_{Vtx} dependence in the jet-veto efficiency is still observed when using the 20 GeV p_T threshold.

7 Track-based Grooming of Large- R jets

At the LHC, many interesting signatures of both Standard Model and new physics processes contain boosted heavy particles, such as W , Z , and H bosons, or top quarks. The successful identification of such topologies requires the use of large- R jets and jet substructure techniques. One of the key ingredients of jet substructure studies is the use of *grooming* techniques (*filtering* [30], *pruning* [31, 32], and *trimming* [33]) that mitigate the effect of pileup on large- R jets. Since pileup effects on the jet p_T are proportional to the area of jets, grooming becomes essential in the case of large- R ($R > 0.6$) jets.

Jet grooming techniques attempt to identify and reject components of large- R jets that are consistent with pileup depositions, effectively reducing the jet area and the sensitivity to pileup. In the case of trimming, for example, $R = 0.3$ k_t subjets with a p_T fraction relative to the parent (ungroomed) jet smaller than $f_{cut} = p_T^{subjet} / p_T^{jet} = 0.05$ are removed.

Building upon the success of calorimeter-based grooming methods and track-based pileup suppression of small- R jets, a new, track-based, grooming technique can be designed by applying corrJVF to the individual subjets of large- R jets. In particular, track-based trimming can be implemented by replacing the f_{cut} criterion with a requirement on the corrJVF of subjets. Other variables, such as JVT or R_{pT} can also be considered, but this note focuses on the use of corrJVF as an example of a purely track-based grooming procedure.

In order to illustrate the concept of track-based grooming, it is useful to consider an event display. Figure 20 shows the rapidity y vs. azimuthal angle ϕ view of a simulated event where a W' boson with a mass of 1 TeV decays to a W and a Z boson, which decay hadronically. The orange star and blue triangle indicate the $y - \phi$ positions of the generated Z and W bosons. The large circles represent the active area boundaries of the anti- k_t $R = 1.0$ jets, built from topological calorimeter clusters [5]. In the following, these jets are referred to as ungroomed jets. The clusters are represented by small solid squares with colors ranging from blue to red encoding low to high transverse energies. The gray regions indicate the active areas of the k_t $R = 0.3$ subjets reconstructed from the constituents of the ungroomed jets. Only subjets with a p_T of at least 5% of the ungroomed jet p_T are shown. Tracks associated with the jet and originating from the hard-scatter vertex (black open circles) or from pileup vertices (black crosses) are also indicated. The violet ungroomed jet (with $\phi \approx 4.1$ and $y \approx -0.2$) has a p_T of 446 GeV and is matched in ΔR to the truth Z boson. While all three subjets have active areas overlapping with the $y - \phi$ positions of pileup tracks, only two subjets have associated hard-scatter tracks. The invariant mass reconstructed from the two subjets with hard-scatter tracks is 89 GeV and the one from all three subjets is 119 GeV. This event display shows that tracking information can provide complementary information to calorimeter-based trimming. Track-assisted trimming would allow the rejection of the third subjet, which is likely to originate from pileup, while keeping the two subjets from the Z boson.

Figure 21 shows the ratio of the subjet p_T and the ungroomed jet p_T on a log-scale as a function of the subjet corrJVF in simulated $W' \rightarrow WZ \rightarrow qqqq$ events. The 2-dimensional distribution is normalized

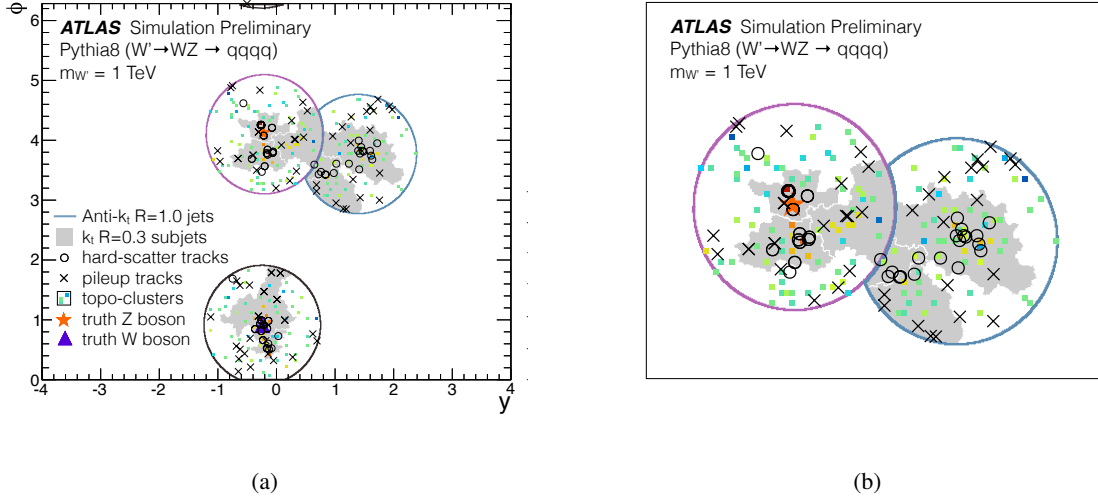


Figure 20: (a) Rapidity - ϕ view of a simulated event of a W' boson with a mass of 1 TeV decaying to a W and a Z . (b) Zoom-in version of (a).

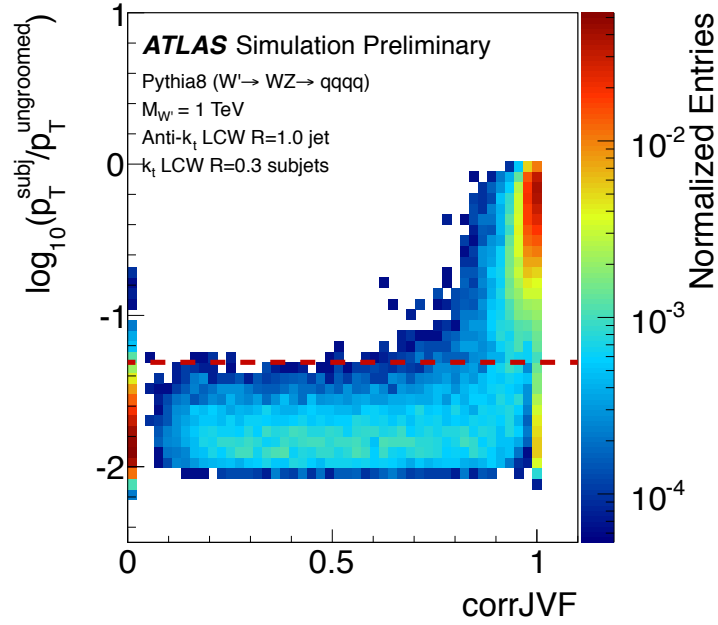


Figure 21: Correlation of subjet p_T fraction and subjet corrJVF for anti- k_t $R = 1.0$ jets with $p_T > 300$ GeV and $|\eta| < 1.5$. The dotted line indicates the standard calorimeter-based trimming p_T ratio cut of 5%. Calorimeter-based trimming would remove all subjets that are below the dotted line, including those with large corrJVF values at the lower right.

to unit area. About 4% of subjects that have no associated tracks ($\text{corrJVF} = -1$) are omitted. Ungroomed jets are selected that have a p_T of at least 300 GeV, $|\eta| < 1.5$, and are matched in ΔR to the truth Z. The corrJVF of the subjects is calculated from the associated hard-scatter and pileup tracks. Most subjects with significant p_T ratio also have large corrJVF , indicating that most of their charged p_T comes from the hard-scatter vertex. A large fraction of subjects with a low p_T ratio $< 5\%$ ($\log_{10}[p_T^{\text{subj}}/p_T^{\text{ungroomed}}] < -1.3$) and a few subjects with a significant p_T ratio, however, have small corrJVF values. Most such subjects are consistent with pileup and should be excluded in a track-based jet grooming procedure. Similarly, subjects with small p_T ratio and large corrJVF that would be removed by calorimeter-based trimming, should be kept by the track-based trimming algorithm.

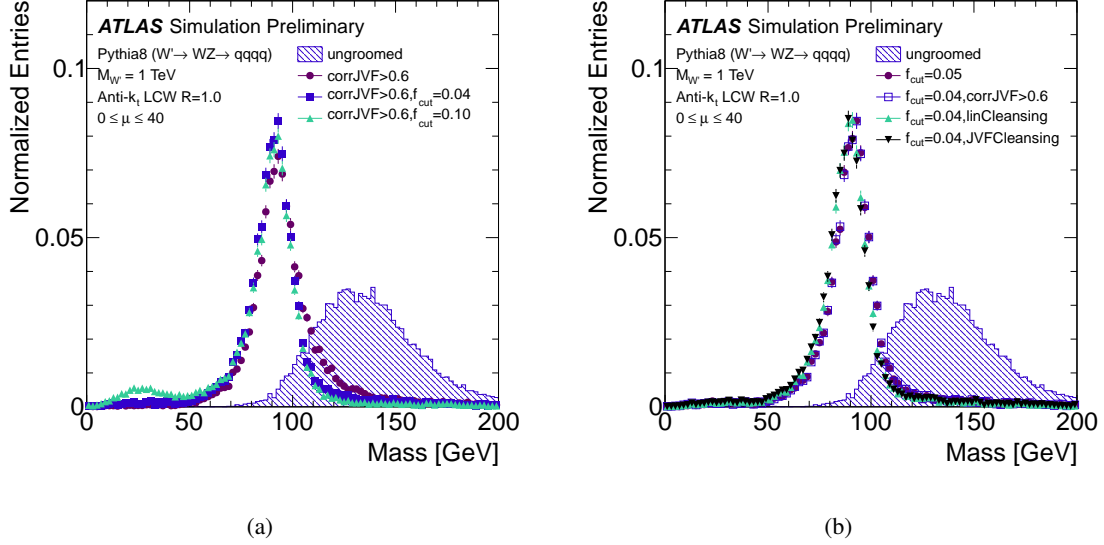


Figure 22: Distribution of the mass of the jet matched to the truth Z boson for different trimming configurations based on corrJVF and f_{cut} . The blue shaded histogram shows the ungroomed jet mass. (a) In the histograms with magenta, blue and green markers, the groomed jet mass is computed from subjects that satisfy a $\text{corrJVF} > 0.6$ requirement, i.e. excluding subjects from pileup interactions. In the blue and green histograms, the subjects are further required to have $p_T^{\text{subj}}/p_T^{\text{ungroomed}}$ (f_{cut}) of at least 4% and 10% respectively. (b) Distribution of jet mass for calorimeter- and track-based trimming configurations and jet cleansing. The histogram represented by magenta markers shows the trimmed jet mass, where the mass is computed from the subjects that have a $p_T^{\text{subj}}/p_T^{\text{ungroomed}}$ of at least 5% ($f_{\text{cut}} = 0.05$). For the green and black histograms, jet cleansing is used.

In Figure 22(a), the performance of track-based grooming is evaluated by comparing the distribution of jet mass for different subject corrJVF cuts and combinations of corrJVF and f_{cut} . The same selection criteria⁷ as in Figure 21 are used for all track-based grooming configurations. For the 2012 pileup conditions with an average of about 21 pp interactions per bunch crossing, an f_{cut} of 4% in addition to the requirement of $\text{corrJVF} > 0.6$ is found to optimize the mass resolution of the groomed jet. A grooming configuration based solely on corrJVF (with no f_{cut} applied) is found to be suboptimal.

Figure 22(b) compares the performance of the track-assisted grooming procedure with a recently proposed jet grooming technique called “jet cleansing” [34]. Standard calorimeter-based trimming with $f_{\text{cut}} = 0.05$ is also shown for reference. In JVF cleansing, the 4-momentum of each subject is scaled by the subject JVF, aiming to approximate the momentum of the subject arising from neutral and charged

⁷The event selection efficiency is about 80% for the considered signal.

particles from the hard-scatter vertex only. In linear cleansing, the subjet 4-momentum from the hard-scatter vertex is approximated by scaling the reconstructed 4-momentum based on the assumption that the ratio of charged to charged plus neutral pileup p_T contributing to a subjet is 0.55. Each f_{cut} used in these procedures is chosen to optimize the mass resolution. For 2012 pileup conditions, the application of track-assisted grooming achieves a similar mass resolution to that of calorimeter-based trimming. No significance difference between corrJVF and jet cleansing is observed. However, for higher luminosity conditions, as expected for the HL-LHC, track-based grooming provides an alternative to calorimeter-only approaches.

8 Conclusions

A new jet-vertex tagging technique, JVT, has been developed for the suppression of pileup jets. The JVT algorithm outperforms the previous JVF algorithm used in ATLAS and solves a fundamental feature of JVF, which is a pileup-dependent jet selection efficiency. The JVT algorithm combines two new pileup-insensitive variables: corrJVF and R_{pT} in a 2-dimensional likelihood. Jet selections based on JVT result in hard-scatter jet efficiencies that are stable within 1% for up to 35 interactions per bunch crossing. This pileup stability also implies that there is no need to re-optimize JVT cut values as pileup conditions change, reducing the dependence on jet reconstruction and the selection of b -tagging and other jet-by-jet tagging techniques. The modeling of JVT was validated in data using $Z(\rightarrow \mu\mu)$ +jets and $t\bar{t}$ events. The jet efficiency was measured in data for three different JVT cut values using a tag and probe method in $Z(\rightarrow \mu\mu)$ +jets events. The efficiencies, measured as a function of p_T and η , are found to agree between data and simulation within 1-2%.

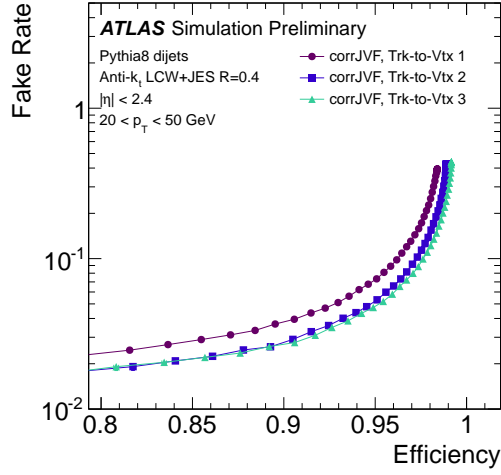
Track-based pileup jet suppression has also been extended to the case of large- R jets by introducing a track-based trimming algorithm that applies a corrJVF selection at the subjet level. The new track-based grooming achieves similar performance to that of calorimeter-based trimming, while using complementary tracking information. The recently proposed jet cleansing grooming technique has also been studied, and results in similar performance to that of all other methods considered.

A Performance details of the track-to-vertex association

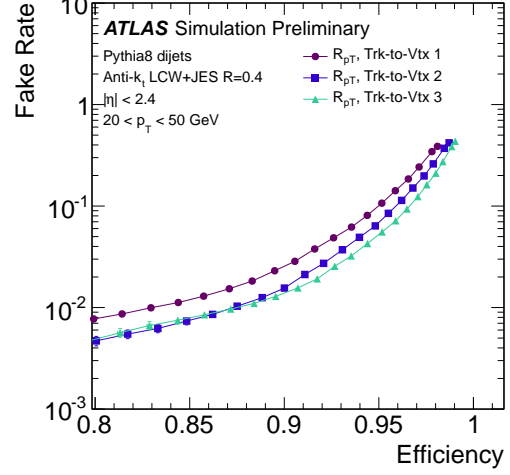
In this note, a track-to-vertex association method is used that is different from the one in Ref. [2]. In Ref. [2], tracks are assigned to vertices by requiring $|\Delta z \times \sin \theta| < 1$ mm. In cases where more than one vertex satisfied this criterion, the ambiguity was resolved by choosing the vertex of higher $\sum_{\text{tracks}} p_T^2$. Here, we chose a different approach:

- Step 1: The vertex reconstruction is used to associate tracks with vertices. If a track is attached to more than one vertex, priority is given to the vertex with higher $\sum_{\text{tracks}} p_T^2$.
- Step 2: If a track is not associated with any primary vertex after step 1, but satisfies $|\Delta z| < 3$ mm with respect to the hard-scatter primary vertex, it is assigned to the hard-scatter primary vertex.

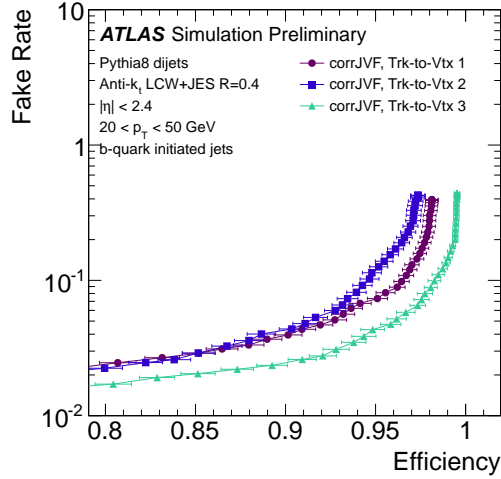
The second step targets tracks from hadron decays in flight originating from the hard-scatter, which are likely not to be attached to any vertex. The $|\Delta z| < 3$ mm criteria was chosen based on the $|z_0|$ distribution of tracks from b -hadron decays, but no strong dependence of the performance on the particular criteria was observed when the cut value was altered within 1 mm. Figure 23(a) and 23(b) show the efficiency versus fake-rate curves comparing the different track-to-vertex association methods, using a sample of $20 < p_T < 50$ GeV jets in simulated QCD dijet events. The new method, labelled “Trk-to-Vtx 3”, shows a significant increase in the hard-scatter jet efficiency at fixed fake rate. The large performance gain for b -quark initiated jets is shown in Figures 23(c) and 23(d).



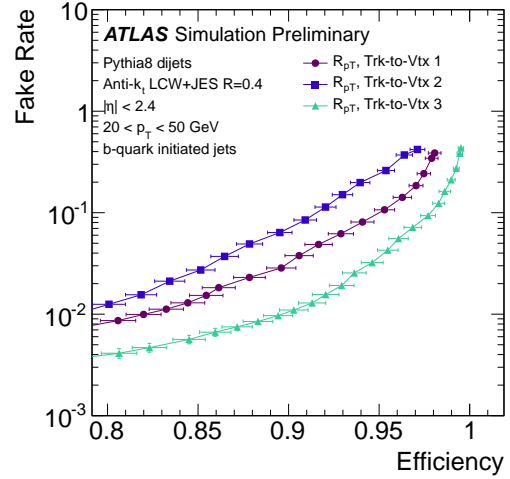
(a)



(b)



(c)



(d)

Figure 23: Fake-rate versus efficiency curves for corrJVF (a) and R_{pT} (b) for three different track-to-vertex associations: the “ $|\Delta z \times \sin \theta| < 1$ mm” criteria labeled “Trk-to-Vtx 1”, “Step 1” labelled “Trk-to-Vtx 2” and the full new procedure “Step 1&2” labelled “Trk-to-Vtx 3”. For b-quark initiated jets, the performance gain for corrJVF (c) and R_{pT} (d) of the new method stems from “Step 2”: without “Step 2” the new method would perform worse than the “ $|\Delta z \times \sin \theta| < 1$ mm” based association.

B Pileup jet rates

Figure 24(a) shows the mean number of pileup jets with $p_T > 20$ GeV per event for two different bin in pseudorapidity: $|\eta| < 2.4$ and $2.4 < |\eta| < 4.5$. No cuts are imposed to suppress pileup jets. An approximately quadratic increase of the pileup jet multiplicity with the average number of interactions per bunch crossing μ is observed. Figure 24(b) shows the pileup jet multiplicity per unit η as a function

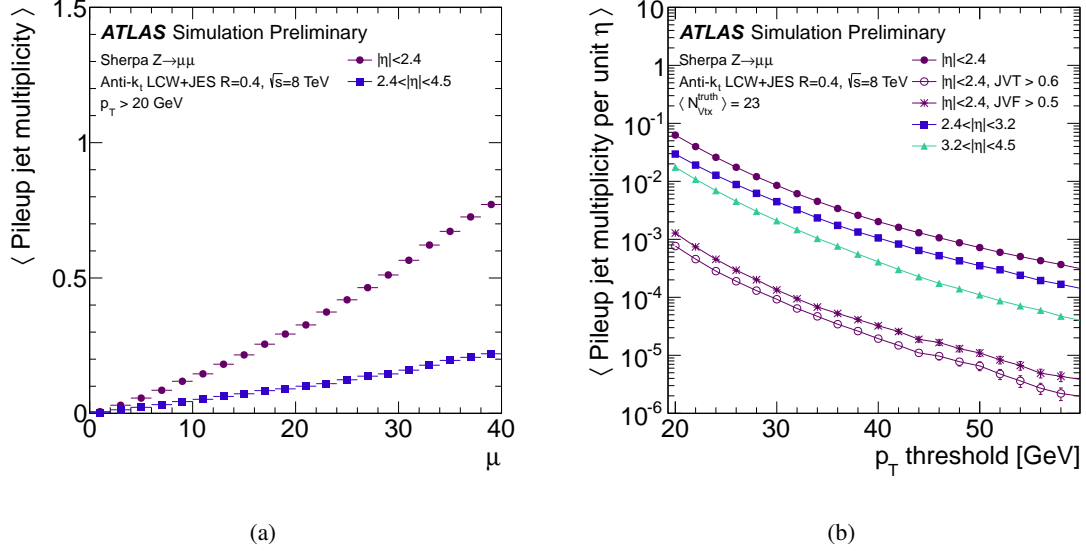


Figure 24: (a) Mean number of pileup jets with $p_T > 20$ GeV as a function of μ . (b) Pileup jet multiplicity per unit η as a function of p_T threshold for different regions of pseudorapidity.

of jet p_T threshold for different η regions. The pileup jet rates in the forward regions of the detector are largely suppressed with respect to the $|\eta| < 2.4$ central region. The graphs with magenta stars and open circles represent respectively the pileup jet rates after imposing $JVF > 0.5$ and $JVT > 0.6$ criteria to suppress pileup jets in the central region. The chosen cut values for JVF and JVT both result in hard-scatter jet efficiencies of about 85% and 90% for jets with $20 < p_T < 30$ GeV and $30 < p_T < 40$ GeV.

C JVT sample dependence

We study the dependence of JVT We test the potential sample dependence of JVT by deriving the JVT likelihood in Fig. 5(a) using a sample of $Z \rightarrow \mu\mu$ events and evaluating its performance in QCD dijet and $Z \rightarrow \mu\mu$ events. The resulting four efficiency vs. fake rate curves are shown in Fig. 25. No significant sample dependence is observed, suggesting that the JVT likelihood in Fig. 5(a) does not underperform when applying it to different physics processes. The difference in the fake rate vs. efficiency curves between Fig. 25(a) and Fig. 25(b) is attributed to the different flavor composition of the jets in QCD dijet and $Z \rightarrow \mu\mu$ events.

References

- [1] ATLAS Collaboration, *The ATLAS Experiment at the CERN Large Hadron Collider*, **JINST** **3** (2008) S08003.

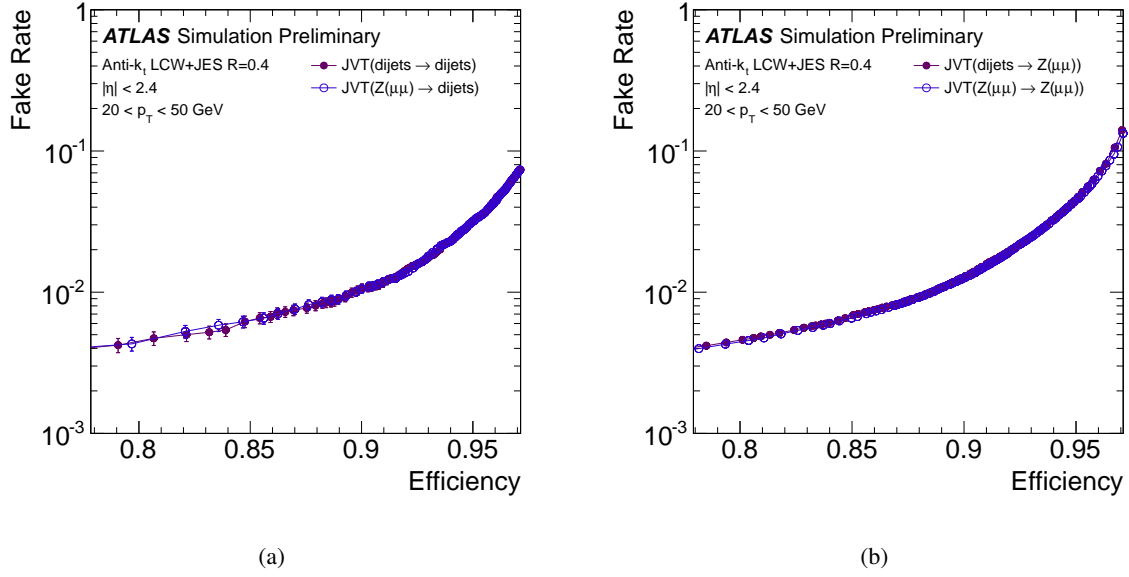


Figure 25: Efficiency vs. fake rate curve for JVT evaluated on $20 < p_T < 50$ GeV jets from a sample of QCD dijet events (a) and $Z \rightarrow \mu\mu$ events (b). The curve represented by solid magenta markers are obtained when deriving the JVT likelihood on a QCD dijet sample. For the open blue markers, the JVT likelihood was derived from $Z \rightarrow \mu\mu$ events. No significant sample dependence is observed.

- [2] ATLAS Collaboration, *Pile-up subtraction and suppression for jets in ATLAS*, ATLAS-CONF-2013-083, 2013.
- [3] ATLAS Collaboration, *Performance of the ATLAS Inner Detector Track and Vertex Reconstruction in the High Pile-Up LHC Environment*, ATLAS-CONF-2012-042, 2012.
- [4] M. Cacciari, G. P. Salam, and G. Soyez, *The Catchment Area of Jets*, **JHEP** **0804** (2008) 005, [arXiv:0802.1188 \[hep-ph\]](#).
- [5] ATLAS Collaboration, *Calorimeter Clustering Algorithms: Description and Performance*, ATL-LARG-PUB-2008-002, 2008.
- [6] ATLAS Liquid Argon EMEC/HEC Collaboration, *Hadronic calibration of the ATLAS liquid argon end-cap calorimeter in the pseudorapidity region $1.6 < |\eta| < 1.8$ in beam tests*, **Nucl. Instrum. Meth. A** **531** (2004) 481–514, [arXiv:physics/0407009 \[physics\]](#).
- [7] M. Cacciari, G. P. Salam, and G. Soyez, *The anti- k_t jet clustering algorithm*, **JHEP** **0804** (2008) 063, [arXiv:0802.1189 \[hep-ph\]](#).
- [8] ATLAS Collaboration, *Jet energy measurement with the ATLAS detector in proton-proton collisions at $\sqrt{s} = 7$ TeV*, **Eur. Phys. J. C** **73** (2013) 2304, [arXiv:1112.6426 \[hep-ex\]](#).
- [9] ATLAS Collaboration, *Jet Charge Studies with the ATLAS Detector Using $\sqrt{s} = 8$ TeV Proton-Proton Collision Data*, ATLAS-CONF-2013-086, 2013.
- [10] ATLAS Collaboration, *Measurement of the b -tag Efficiency in a Sample of Jets Containing Muons with 5 fb^{-1} of Data from the ATLAS Detector*, ATLAS-CONF-2012-043, 2012.

- [11] S. Alioli, P. Nason, C. Oleari, and E. Re, *A general framework for implementing NLO calculations in shower Monte Carlo programs: the POWHEG BOX*, **JHEP** **1006** (2010) 043, [arXiv:1002.2581 \[hep-ph\]](#).
- [12] S. Frixione, P. Nason, and C. Oleari, *Matching NLO QCD computations with Parton Shower simulations: the POWHEG method*, **JHEP** **0711** (2007) 070, [arXiv:0709.2092 \[hep-ph\]](#).
- [13] P. Nason, *A New method for combining NLO QCD with shower Monte Carlo algorithms*, **JHEP** **0411** (2004) 040, [arXiv:hep-ph/0409146 \[hep-ph\]](#).
- [14] H.-L. Lai, M. Guzzi, J. Huston, Z. Li, P. M. Nadolsky, et al., *New parton distributions for collider physics*, **Phys. Rev.** **D82** (2010) 074024, [arXiv:1007.2241 \[hep-ph\]](#).
- [15] T. Sjostrand, S. Mrenna, and P. Z. Skands, *PYTHIA 6.4 Physics and Manual*, **JHEP** **0605** (2006) 026, [arXiv:hep-ph/0603175 \[hep-ph\]](#).
- [16] P. Z. Skands, *Tuning Monte Carlo Generators: The Perugia Tunes*, **Phys. Rev.** **D82** (2010) 074018, [arXiv:1005.3457 \[hep-ph\]](#).
- [17] J. Pumplin, D. Stump, J. Huston, H. Lai, P. M. Nadolsky, et al., *New generation of parton distributions with uncertainties from global QCD analysis*, **JHEP** **0207** (2002) 012, [arXiv:hep-ph/0201195 \[hep-ph\]](#).
- [18] B. P. Kersevan and E. Richter-Was, *The Monte Carlo event generator AcerMC versions 2.0 to 3.8 with interfaces to PYTHIA 6.4, HERWIG 6.5 and ARIADNE 4.1*, **Comput. Phys. Commun.** **184** (2013) 919–985, [arXiv:hep-ph/0405247 \[hep-ph\]](#).
- [19] T. Gleisberg, S. Hoeche, F. Krauss, M. Schonherr, S. Schumann, et al., *Event generation with SHERPA 1.1*, **JHEP** **0902** (2009) 007, [arXiv:0811.4622 \[hep-ph\]](#).
- [20] T. Sjostrand, S. Mrenna, and P. Z. Skands, *A Brief Introduction to PYTHIA 8.1*, **Comput. Phys. Commun.** **178** (2008) 852–867, [arXiv:0710.3820 \[hep-ph\]](#).
- [21] M. L. Mangano, M. Moretti, F. Piccinini, R. Pittau, and A. D. Polosa, *ALPGEN, a generator for hard multiparton processes in hadronic collisions*, **JHEP** **0307** (2003) 001, [arXiv:hep-ph/0206293 \[hep-ph\]](#).
- [22] ATLAS Collaboration, *Summary of ATLAS Pythia 8 tunes*, ATL-PHYS-PUB-2012-003, 2012.
- [23] A. Martin, W. Stirling, R. Thorne, and G. Watt, *Parton distributions for the LHC*, **Eur. Phys. J.** **C63** (2009) 189–285, [arXiv:0901.0002 \[hep-ph\]](#).
- [24] ATLAS Collaboration, *The ATLAS Simulation Infrastructure*, **Eur. Phys. J.** **C70** (2010) 823–874, [arXiv:1005.4568 \[physics.ins-det\]](#).
- [25] GEANT4 Collaboration, S. Agostinelli et al., *GEANT4: A Simulation toolkit*, **Nucl. Instrum. Meth.** **A506** (2003) 250–303.
- [26] A. Hoecker, P. Speckmayer, J. Stelzer, J. Therhaag, E. von Toerne, and H. Voss, *TMVA: Toolkit for Multivariate Data Analysis*, PoS ACAT (2007) 040, [arXiv:physics/0703039](#).
- [27] ATLAS Collaboration, *Light-quark and Gluon Jets: Calorimeter Response, Jet Energy Scale Systematics and Properties*, ATLAS-CONF-2012-138, 2012.
- [28] CMS Collaboration, *Pileup Jet Identification*, CMS-PAS-JME-13-005, 2013.

- [29] ATLAS Collaboration, *Measurements of the properties of the Higgs-like boson in the four lepton decay channel with the ATLAS detector using 25 fb^{-1} of proton-proton collision data*, ATLAS-CONF-2013-013, 2013.
- [30] J. M. Butterworth, A. R. Davison, M. Rubin, and G. P. Salam, *Jet substructure as a new Higgs search channel at the LHC*, *Phys. Rev. Lett.* **100** (2008) 242001, [arXiv:0802.2470 \[hep-ph\]](#).
- [31] S. D. Ellis, C. K. Vermilion, and J. R. Walsh, *Techniques for improved heavy particle searches with jet substructure*, *Phys. Rev.* **D80** (2009) 051501, [arXiv:0903.5081 \[hep-ph\]](#).
- [32] S. D. Ellis, C. K. Vermilion, and J. R. Walsh, *Recombination Algorithms and Jet Substructure: Pruning as a Tool for Heavy Particle Searches*, *Phys. Rev.* **D81** (2010) 094023, [arXiv:0912.0033 \[hep-ph\]](#).
- [33] D. Krohn, J. Thaler, and L.-T. Wang, *Jet Trimming*, *JHEP* **1002** (2010) 084, [arXiv:0912.1342 \[hep-ph\]](#).
- [34] D. Krohn, M. Low, M. D. Schwartz, and L.-T. Wang, *Jet Cleansing: Pileup Removal at High Luminosity*, [arXiv:1309.4777 \[hep-ph\]](#).